GFDL's CM2 Global Coupled Climate Models. Part II: The Baseline Ocean Simulation

ANAND GNANADESIKAN,* KEITH W. DIXON,* STEPHEN M. GRIFFIES,* V. BALAJI,+ MARCELO BARREIRO,+ J. ANTHONY BEESLEY,# WILLIAM F. COOKE,@,** THOMAS L. DELWORTH,* RUDIGER GERDES,& MATTHEW J. HARRISON,* ISAAC M. HELD,* WILLIAM J. HURLIN,* HYUN-CHUL LEE,@,** ZHI LIANG,@,** GIANG NONG,@,** RONALD C. PACANOWSKI,* ANTHONY ROSATI,* JOELLEN RUSSELL,+ BONITA L. SAMUELS,* QIAN SONG,+ MICHAEL J. SPELMAN,* RONALD J. STOUFFER,* COLM O. SWEENEY,+ GABRIEL VECCHI,# MICHAEL WINTON,* ANDREW T. WITTENBERG,* FANRONG ZENG,@,** RONG ZHANG,+ AND JOHN P. DUNNE*

*NOAA/Geophysical Fluid Dynamics Laboratory, Princeton, New Jersey
+ Program in Atmospheric and Oceanic Sciences, Princeton University, Princeton, New Jersey
# UCAR Visiting Scientist Program, NOAA/Geophysical Fluid Dynamics Laboratory, Princeton, New Jersey
@ RS Information Systems, Inc., McLean, Virginia
& Alfred Wegener Insitute for Polar and Marine Research, Bremerhaven, Germany

(Manuscript received 23 January 2005, in final form 15 June 2005)

ABSTRACT

The current generation of coupled climate models run at the Geophysical Fluid Dynamics Laboratory (GFDL) as part of the Climate Change Science Program contains ocean components that differ in almost every respect from those contained in previous generations of GFDL climate models. This paper summarizes the new physical features of the models and examines the simulations that they produce. Of the two new coupled climate model versions 2.1 (CM2.1) and 2.0 (CM2.0), the CM2.1 model represents a major improvement over CM2.0 in most of the major oceanic features examined, with strikingly lower drifts in hydrographic fields such as temperature and salinity, more realistic ventilation of the deep ocean, and currents that are closer to their observed values. Regional analysis of the differences between the models highlights the importance of wind stress in determining the circulation, particularly in the Southern Ocean. At present, major errors in both models are associated with Northern Hemisphere Mode Waters and outflows from overflows, particularly the Mediterranean Sea and Red Sea.

1. Introduction

A major part of developing a "realistic" model of the climate system is the development of a model of ocean circulation. The ocean circulation plays an important role in the earth's climate. By transporting heat to polar latitudes, it plays a major role in maintaining the habitability of such regions (Manabe and Bryan 1969). Ocean heat transport plays a major role in determining the extent of sea ice (Winton 2003), which has a major effect on planetary albedo. Manabe et al. (1991) and Stouffer (2004) show that the ocean determines the spatial pattern and temporal scale of response to changes in the surface radiation balance. However, despite many decades of research, different ocean general circulation models still yield solutions that differ in important ways. Recent work as part of the Ocean Carbon Model Intercomparison Project (OCMIP), which involved comparisons between ocean-only models run by 13 groups, showed large differences in overturning streamfunction (Doney et al. 2004) and the rate of ventilation in the Southern Ocean (Matsumoto et al. 2004). Such differences have important implications for climate change. For example, models that maintain high levels of convection in the Southern Ocean may also have too strong a response to an increase in the hydrological cycle, cutting off convection that does not exist in the real world. Such differences could have major implications for ocean ecosystems, which are very dependent on the rate of vertical exchange (Gnanadesi-

** Current affiliation: NOAA/Geophysical Fluid Dynamics Laboratory, Princeton, New Jersey.

Corresponding author address: Dr. Anand Gnanadesikan, NOAA/Geophysical Fluid Dynamics Laboratory, P.O. Box 308, Forrestal Campus, Princeton, NJ 08542.
E-mail: Anand.Gnanadesikan@noaa.gov

© 2006 American Meteorological Society

kan et al. 2002) and for the response of the carbon cycle to climate change (Sarmiento et al. 1998).

Understanding such issues is particularly challenging in ocean models because of questions about the impact of numerics. Processes known to have an important impact on vertical exchange in level-coordinate models include numerical diffusion resulting from truncation errors associated with advection (Griffies et al. 2000), truncation errors associated with isopycnal mixing (Griffies et al. 1998), convective entrainment in overflows (Winton et al. 1998), and high levels of background lateral diffusion. The past decade has seen sustained effort in the modeling community at large to address some of the more egregious numerical shortcomings in models. At the Geophysical Fluid Dynamics Laboratory (GFDL), we have developed a new ocean code, the Modular Ocean Model Version 4.0 (MOM4; Griffies et al. 2003) in which almost every aspect of the ocean model from the free surface to the bottom boundary has been revisited.

This new code has been used to configure two models that are run as part of the global climate coupled models versions 2.0 and 2.1 (CM2.0 and CM2.1; Delworth et al. 2006). While the ocean components of the two models are very similar, differing only in a few subgrid-scale parameterizations and in the time-stepping scheme, the atmospheric components are substantially different, resulting in significant differences in the distribution of wind stress. While the ocean-only versions of these models are referred to at GFDL by the nomenclature OM3.0 (for the ocean component used in CM2.0) and OM3.1 (for the ocean component used in CM2.1) in this paper we will simply identify the ocean components by the coupled model of which they are a part (since we will only be presenting solutions from these coupled models). This paper examines the ocean circulation produced by the CM2.0 and CM2.1 coupled models. In particular, it looks at the following questions:

1) What are the principal errors in hydrography and flow fields made by the models?
2) How do these errors differ between CM2.0 and CM2.1?
3) What mechanisms and processes can account for common errors and explain differences between the models?

Our goal is both to document lessons learned from running the pair of models and to highlight areas where the model circulation is greatly in error. In the latter case, we note that it would be unwise for other investigators to draw strong conclusions about the effects of climate change based on features that are not well simulated. Section 2 gives a brief description of the numerical formulation of the ocean model. Section 3 looks at global diagnostics of the simulation. Section 4 examines some diagnostics of the circulation in five regions; the Southern Ocean, the North Atlantic, the North Pacific, the northern Indian Ocean, and the Arctic. The tropical Pacific (which is well represented in both models) is discussed in detail in the companion paper of Wittenberg et al. (2006, hereafter Part III), the variability in the tropical Indian Ocean is discussed in Song et al. (2005, manuscript submitted to *J. Climate*, hereafter SVR), and the tropical Atlantic will be discussed in a paper by M. Barreiro et al. (2005, unpublished manuscript). Section 5 looks at reasons for the changes between the models. Section 6 concludes this paper.

2. Model formulation

a. Common features of the models

The GFDL ocean model presented here differs significantly from that used in previous assessments. A summary of the differences is provided below. For a more detailed discussion of the model formulation the reader is referred to Griffies et al. (2005).

The ocean model is of significantly higher resolution than the 4°, 12-level model (Manabe et al. 1991) used in the IPCC First Assessment Report (1990) and the 2°, 18-level model (Delworth et al. 2002) used in the Third Assessment Report (2001). The longitudinal resolution of the CM2 series is 1° and the latitudinal resolution varies between 1° in the midlatitudes and 1/3° in the Tropics, where higher resolution was needed to resolve the equatorial waveguide. A tripolar grid (Murray 1996) is used to move the polar singularity onto the land, allowing for resolved cross-polar flow and eliminating the necessity to filter fields near the pole. There are 50 vertical levels with 22 uniformly spaced over the top 220 m. Below this depth, the grid box thickness increases gradually to a value of 366.6 m in the deepest parts of the ocean, with a maximum depth of 5500 m.

In contrast to previous models that used the rigid-lid approximation to solve for the surface pressure, the CM2 models use an explicit free surface (Griffies et al. 2001). This allows for real fluxes of freshwater, in contrast to the "virtual salt fluxes" used by most ocean models. However, the use of real freshwater fluxes introduces a number of new problems. The first is that the free surface thins when water freezes into sea ice. This can result in numerical instability when the thickness of sea ice approaches the thickness of the top box. In the CM2 models this is solved by limiting the ice weight on the ocean to 4 m of ice even when the ice thickness exceeds 4 m. Second, rivers must be handled

in a special way, inserting fluid into the ocean instead of fluxing salt. Third, narrow passages that connect marginal seas to the main body of the ocean, which in past models were represented by stirring fluid between boxes separated by land, must allow for a net flow of mass to prevent excessive buildup or drawdown of water in these otherwise isolated basins. Finally, using a real freshwater flux can result in nonconservation of certain tracers when traditional leapfrog time-stepping schemes are used. More discussion of these issues is provided in Griffies et al. (2005).

The models also incorporate a number of improvements in upper-ocean physics. The mixed layer is predicted using the K-profile parameterization (KPP) mixed layer scheme of Large et al. (1994). Shortwave radiation absorption is represented using the optical model of Morel and Antoine (1994) with a yearly climatological concentration of chlorophyll from the Sea-Viewing Wide Field-of-View Sensor (SeaWIFS) satellite. The principal impact of including variable penetration of shortwave radiation is found in the Tropics in ocean-only models (Sweeney et al. 2005).

The representation of near-bottom processes has also been improved in the CM2 model series. Bottom topography is represented using the method of partial cells (Adcroft et al. 1997; Pacanowski and Gnanadesikan 1998) and is thus much less sensitive to the details of vertical resolution. Better representation of the details of bottom topography does not, however, solve one of the most persistent problems of level-coordinate models, namely the tendency to dilute sinking plumes of dense water (Winton et al. 1998). To ameliorate the effects of this "convective entrainment," a primitive representation of bottom boundary layer processes (following Beckmann and Döscher 1997) has been added in which fluid is mixed along the slope when dense water is found upslope of light water.

The interaction of tides with the ocean bottom can serve as a major driver of mixing. In shallow regions, large tidal velocities can directly generate high levels of turbulence. In the CM2 model series, this effect was parameterized by adding a source of turbulent kinetic energy based on a global model of tides to the bottommost level in the KPP scheme. More details are presented in Lee et al. (2006). They show that tidal mixing resulted in a substantial reduction in Arctic stratification and helped to reduce excessively low salinities at certain river mouths. However, it did not have a major impact on the overturning circulation or on temperature drifts.

The interaction of tides with the ocean bottom can also produce internal waves that propagate upward in the water column and break. Because the deep ocean is less stratified than the pycnocline, this produces relatively high levels of vertical dissipation in the deep ocean (Polzin et al. 1997). For many years, GFDL models have attempted to represent this effect by having the vertical diffusion transition between a relatively low value (0.15–0.3 $cm^2\ s^{-1}$) in the pycnocline and a relatively high value (1.0–1.3 $cm^2\ s^{-1}$) in the deep ocean (Bryan and Lewis 1979). The present model uses the same pycnocline value of 0.3 $cm^2\ s^{-1}$ as previous models poleward of 40° in both hemispheres, with a lower value of 0.15 $cm^2\ s^{-1}$ in the low latitudes. The lower tropical value is clearly justified by the results of the North Atlantic Tracer Release Experiment (Ledwell et al. 1993), by turbulence profiling along the equator (Peters et al. 1988), and by simulations showing that such a high value of turbulent diffusion can lead to excessive deep upwelling at the equator (Gnanadesikan 1999; Gnanadesikan et al. 2002). An even higher value of vertical diffusion than the one we have used may be justified within the Southern Ocean where internal wave activity is known to be enhanced (Polzin 1999), but the value used in the Arctic is likely still too high, given that internal wave activity is known to be very low there (Levine et al. 1985). A value of 1.2 $cm^2\ s^{-1}$ is used in the deep ocean. While some recent schemes (Simmons et al. 2004) allow for deep mixing to be spatially variable, they were not judged mature enough for inclusion into this version of the coupled model when the model formulation was frozen.

In addition to lowering the vertical mixing in the subtropical thermocline, a number of other changes were made to the physics in the model interior. One is that the advection scheme was changed from the centered-difference scheme used in previous versions of the model to the flux-corrected scheme utilized in the Massachusetts Institute of Technology (MIT) general circulation model. This scheme is based on the third-order upwind-biased approach of Hundsdorfer and Trompert (1994), which employs the flux limiters of Sweby (1984) to ensure that tracers do not go out of bounds. Additionally, the lateral mixing of both tracers and momentum is considerably more sophisticated than in previous versions of the model. Because there are important differences in how the lateral mixing is implemented between CM2.0 and CM2.1, we discuss these separately in two sections below.

b. Isoneutral mixing parameterization

There are two key characteristics of the mixing associated with eddies. First, eddies within the ocean interior tend to homogenize tracers along surfaces of constant neutral density (Ledwell et al. 1998). In numerical models of ocean circulation one of the tracers that tends to be homogenized in this way is potential vor-

ticity (PV; Rhines and Young 1982). On a flat f-plane, PV homogenization corresponds to an advective flow that homogenizes interface heights. Such flows are parameterized in CM2 according to the parameterization of Gent and McWilliams (1990, henceforth GM) as implemented by Griffies (1998). Essentially, one can think of eddies as leading to an advective flow given by

$$M = -(\partial/\partial z)(\kappa S), \tag{1}$$

where κ is a diffusive coefficient and S is the isopycnal slope. Completing the closure requires a closure for dealing with κ, particularly as S goes to infinity in the mixed layer.

In CM2.0 and CM2.1 κ is a function of the horizontal density gradient averaged over the depth range of 100 to 2000 m. The formula for κ is

$$\kappa = \alpha \overline{|\nabla_z \rho|}^z \left(\frac{L^2 g}{\rho_o N_o} \right). \tag{2}$$

Here, α is a dimensionless tuning constant set to 0.07, L is a constant length scale set to 50 km, N_o is a constant buoyancy frequency set to 0.004 s^{-1}, $g = 9.8$ m s^{-1} is the acceleration of gravity, $\rho_o = 1035$ kg m^{-3} is the reference density for the Boussinesq approximation, and $\overline{|\nabla_z \rho|}^z$ is the average of the horizontal density gradient (i.e., the baroclinicity) taken over the depth range 100 to 2000 m. Maximum and minimum values are set to 600 and 100 m^2 s^{-1}, respectively. Effectively, this produces high values of κ in boundary currents, low values in the ocean interior, and moderately high values in convective regions that are weakly stratified. Within the mixed layer, κS is interpolated between the value at the mixed layer base and a value of 0 at the surface. When the absolute value of the slope is greater than 0.002, it is reduced to 0.002 for purposes of the GM parameterization. Figure 1 shows a map of κ in CM2.0.

In CM2.0 the isopycnal mixing coeffficient A_I is identical to κ. In CM2.1 it is maintained at a value of 600 m^2 s^{-1} throughout the ocean. This difference was found to reduce sea ice biases, particularly in the North Pacific (see Griffies et al. 2005, their Fig. 12; Delworth et al. 2006, their Fig. 15). While it has a relatively small effect on the overall model solution (as discussed below in section 5), this choice represents an attempt to tune away a model bias, rather than an attempt to make a poorly represented process more physical. It is interesting to note that the Hadley Centre and L'Institut Pierre-Simon Laplace (IPSL) models handle κ and A_I in a similar manner (Guilyardi et al. 2001; Johns et al. 2005).

c. Lateral viscosity parameterization

Lateral viscosity is used in climate models to produce a Munk boundary layer and to smooth out unphysical noise produced by the advection equation. This requires large values of viscosity, particularly in the east–west direction, of order 10^5 m^2 s^{-1}. These values are much larger than the diffusivities and are not thought to be physically realistic. Such large viscosities, however, tend to broaden and slow the equatorial undercurrent, with implications for important climate modes such as El Niño. In CM2.0 and CM2.1 we adopt an anisotropic viscosity scheme in tropical latitudes. This scheme is similar to that of Large et al. (2001), which produces large viscosity in the east–west direction, but relatively small viscosity in the north–south direction outside of boundary currents. Outside of the Tropics, the background viscosity is isotropic. The viscosity schemes are identical in the two models in the Tropics, but in CM2.1 the isotropic background viscosity was reduced in the extratropics so as to generate more vigorous extratropical boundary currents. Again, changes in the circulation resulting from this difference should be seen as a statement about the sensitivity of the models, rather than about the details of the real ocean. Figure 2 shows the east–west and north–south viscosities in the two models.

d. Time stepping

As in the MOM2 and MOM3 models, the ocean code used in CM2.0 was integrated forward in time using a leapfrog time step. While such a scheme is simple, it is also very unstable, requiring the use of filtering to eliminate computational modes. In the presence of an explicit free surface, such filtering introduces nonconservative terms in the tracer equation, which although very small, are nonzero (Griffies et al. 2001). Moreover, using a leapfrog time step requires keeping track of two sets of solutions (on odd and even time steps). However, the maximum allowable time step is that which results in instability when integrating the equations on the odd (or even) time steps using forward integration. By switching to a more sophisticated forward integration one can eliminate one set of solutions, greatly increasing the speed of the model. This was done in CM2.1. Changing the time-stepping scheme has a small impact on the solution in most parts of the model, though some changes are seen right on the equator. More discussion of this issue is provided in Griffies et al. (2005).

e. Simulation protocol

The simulations are initialized from the *World Ocean Atlas 2001* (Stephens et al. 2002; Boyer et al. 2002) data for temperature and salinity. Two sets of control runs are done, one using 1990s radiative conditions where the net ocean heating is around 1 W m^{-2} and one using

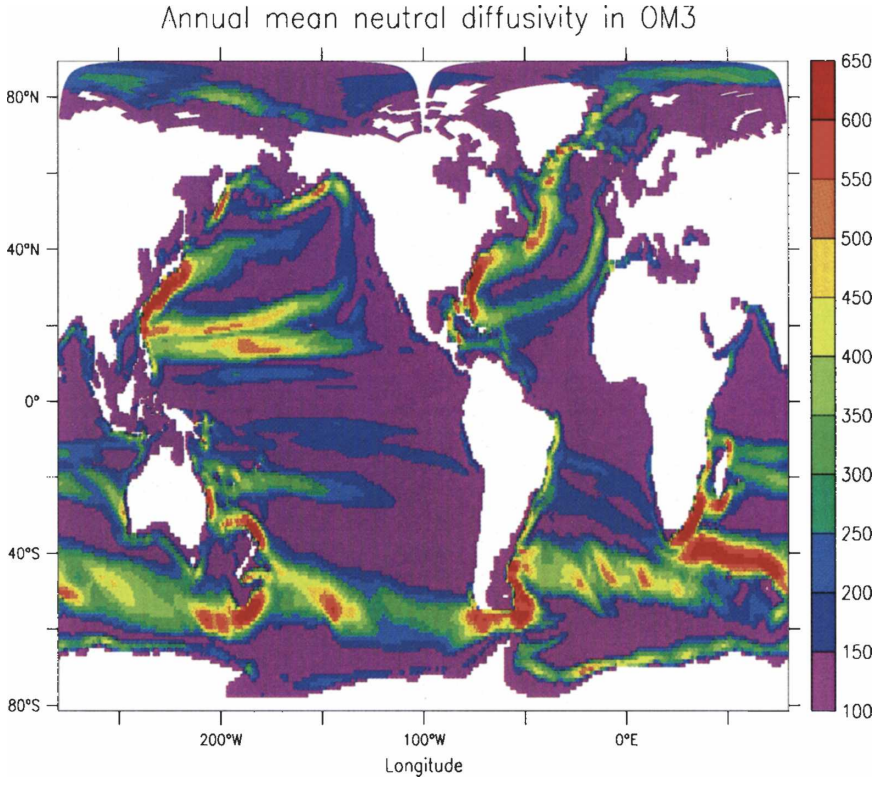

FIG. 1. Thickness diffusion coefficient κ in $m^2\ s^{-1}$ in CM2.0.

1860s radiative conditions with a net ocean heating of 0.3 W m^{-2} (see Fig. 3 of Delworth et al. 2006). In previous versions of the GFDL coupled model, the atmosphere was spun up for many years using prescribed sea surface temperatures, the ocean was spun up over many years using the output of the atmospheric model, and flux adjustments were computed by restoring the surface temperatures and salinities to observations within the ocean-only model. The combined model was then coupled. In the present series of models this is not done. Instead, the models are essentially initialized from initial conditions and allowed to drift without flux adjustments.

One of the drawbacks of this approach is that it is not clear how to compare the model with observations. Modern observations have been taken during a period when the climate has a trend. The model may or may not be in a similar balance. Since the data are largely modern, we decided to present simulations from our 1990 control runs, which as documented in Delworth et al. (2006) have relatively little drift in sea surface temperatures. For the main body of the paper, we present results from years 101–200 of these control runs, with the exception of the ideal age, where years 65–70 are used to facilitate comparison with observations.

Additionally, we compare differences between CM2.1 and CM2.0 with two simulations run as part of the model development process with the CM2.1 atmosphere. The first of these simulations is identical to CM2.1 except that it has a lower viscosity as in CM2.0. In the second run both the isopycnal mixing and viscosity are as in CM2.0. These runs are used to evaluate whether the differences between the CM2.0 and CM2.1 simulations are primarily due to changes in the atmosphere or in the ocean. Years 20–60 of these runs are used and compared with the identical time periods from CM2.0 and CM2.1.

3. Global-scale diagnostics

Temperature and salinity are the best-known oceanic fields. Because the interior flow is to a large extent geostrophic and thus controlled by the density field, temperature and salinity errors are often reflected in errors in flow as well. That the surface temperature and salinity errors are much lower in CM2.1 than CM2.0 has already been shown (Delworth et al. 2006). Similar improvement is seen in many parts of the water column. One way to see this in more detail is to look at the rms temperature and salinity errors averaged over the top 1500 m (Fig. 3).

The temperature errors in CM2.0 are distributed

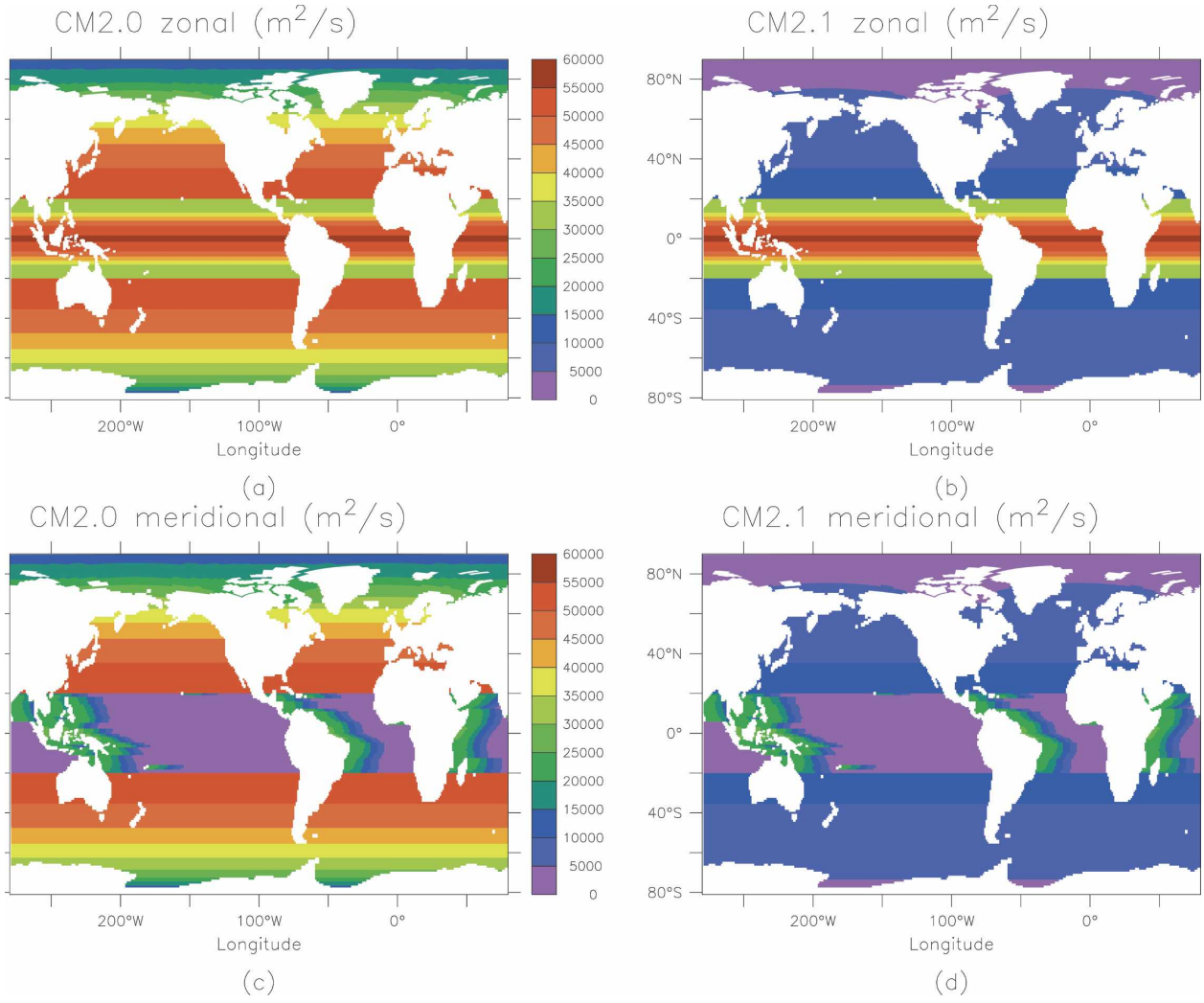

FIG. 2. Time-independent viscosities in $m^2\ s^{-1}$ used in the CM2 series at the ocean surface. Zonal viscosity in (a) CM2.0 and (b) CM2.1. Meridional viscosity in (c) CM2.0 and (d) CM2.1.

across many regions, with the North Atlantic (25% of the error variance) followed closely by the errors associated with the details of the subtropical gyre in the South Pacific (21% of the error variance) and with mode water formation in the North Pacific (16% of the error variance). The Arabian Sea (4.5% of the temperature error variance) also stands out. By contrast, the error variance in CM2.1 is primarily found in the Northern Hemisphere, with the North Atlantic accounting for 41% of the temperature error variance. The temperature error variance in the South Pacific has dropped by a factor of 3, and that in the North Pacific by 25%. Similarly, there are significant improvements in the rms salinity errors in the Southern Hemisphere, which drop from 0.25 to 0.20 PSU. A smaller drop is seen in the Northern Hemisphere (from 0.42 to 0.40). A basic analysis of these improvements is given in section 4 with a more detailed analysis in forthcoming papers (Russell et al. 2005, manuscript submitted to *J. Climate*, hereafter RGT).

Another interesting measure of hydrography is the pycnocline depth. Following Park and Bryan (2000), the pycnocline depth D_{pyc} is defined as

$$D_{\text{pyc}} = \frac{2\int[\sigma_2(z) - \sigma_2(z = 2500)]z\,dz}{\int[\sigma_2(z) - \sigma_2(z = 2500)]\,dz}. \qquad (3)$$

So defined, the pycnocline depth may be thought of as a lower limit of the lightest waters. If the density profile is given by an exponential profile, D_{pyc} is twice the *e*-folding scale. If it is characterized by a single sharp discontinuity between light and dense water, D_{pyc} is the

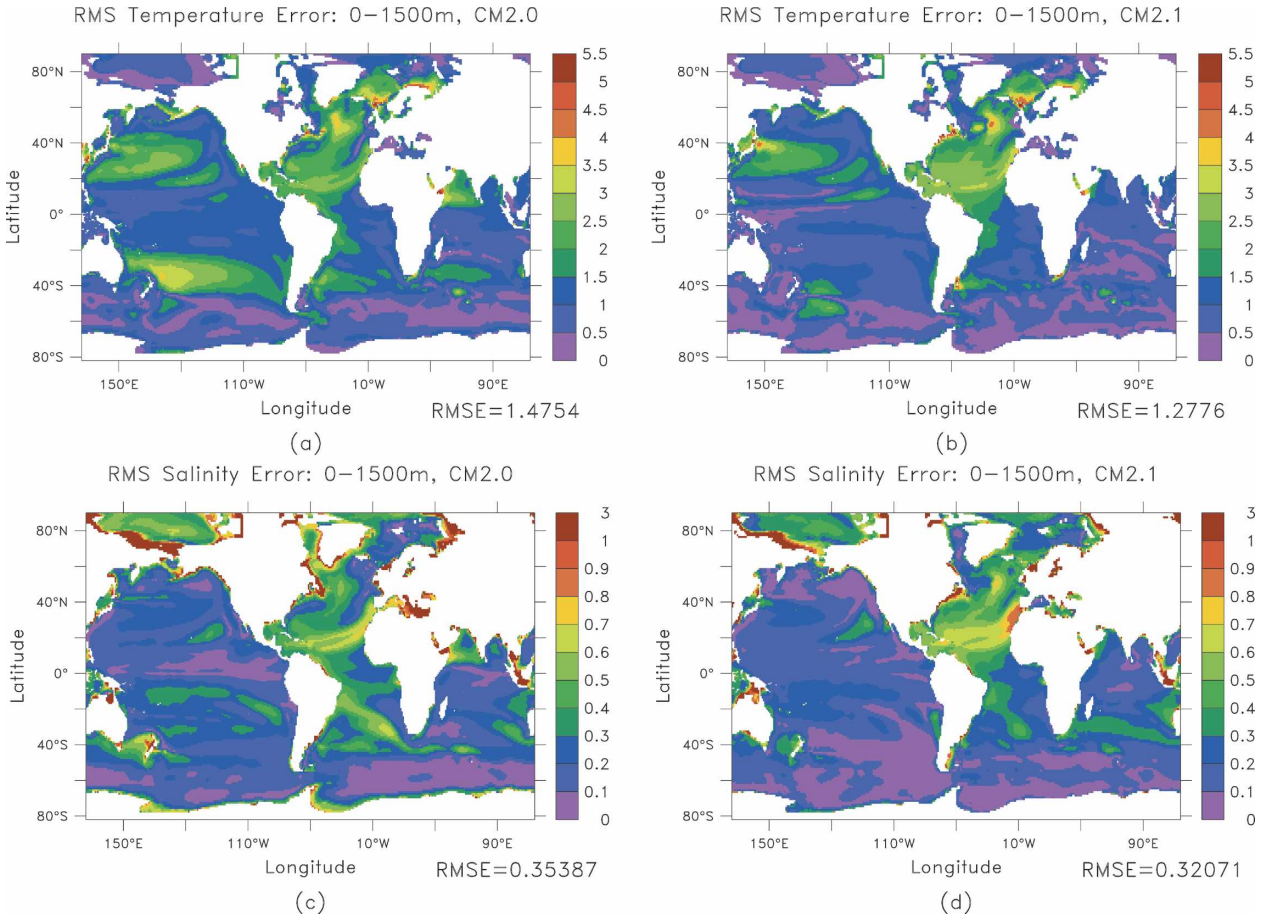

FIG. 3. Rms errors over the top 1500 m relative to the *World Ocean Atlas 2001*. Temperature error in °C for (a) CM2.0 and (b) CM2.1. Salinity error in PSU for (c) CM2.0 and (d) CM2.1.

depth of that discontinuity. The observed D_{pyc} (Fig. 4a) is shallowest (≈400 m) in the Arctic, is deepest in the mode water formation regions in the Southern Ocean, and has intermediate values of around 800 m in the Tropics. It is actually shallower in the western portion of the gyres (where warm water is closest to the surface). The models (Figs. 4b and 4c) reproduce many features of the observations, particularly in the tropical Pacific. Differences are found in the Southern Ocean, where the pycnocline depth in the mode and intermediate water formation regions is too shallow. Additional differences are seen in the details of convective regions in high latitudes, which can be shifted relative to their observed locations. This is one reason that the correlation between observed and modeled pycnocline depths are relatively low (0.66 and 0.65). Correlations rise significantly (to 0.75 and 0.78, respectively) when only the Tropics are considered. The excessive depth of the Arctic pycnocline appears to be related to the surface pressure and wind stress, which is excessively anticyclonic. The large change in pycnocline depth in the Weddell Sea is due to the persistence of open-ocean convection within this region in CM2.1, as opposed to the rather intermittent and shallow convection seen in CM2.0.

While sea surface height (compared in Fig. 5 with the first year of the TOPEX-Poseidon altimeter; Tapley et al. 1994) mirrors the pycnocline, the agreement with observations is much better. The model captures the bulk of variability, with very low values (less than −1.6 m) in the far Southern Ocean, intermediate values (ranging from −0.4 to 0.4 m) in the Atlantic, moderately high values (0.6–0.8 m) in the Indian, and the highest values in the Pacific. The zonal average (Fig. 5d) is extremely consistent between the models and the data with the exception of the far North Atlantic. The principal differences are associated with large signals in marginal seas. We note that because MOM4 uses an explicit free surface, we can compare the model sea surface height with observations.

The overturning streamfunction in depth space (Figs. 6a,c) is dominated by the pole-to-pole circulation asso-

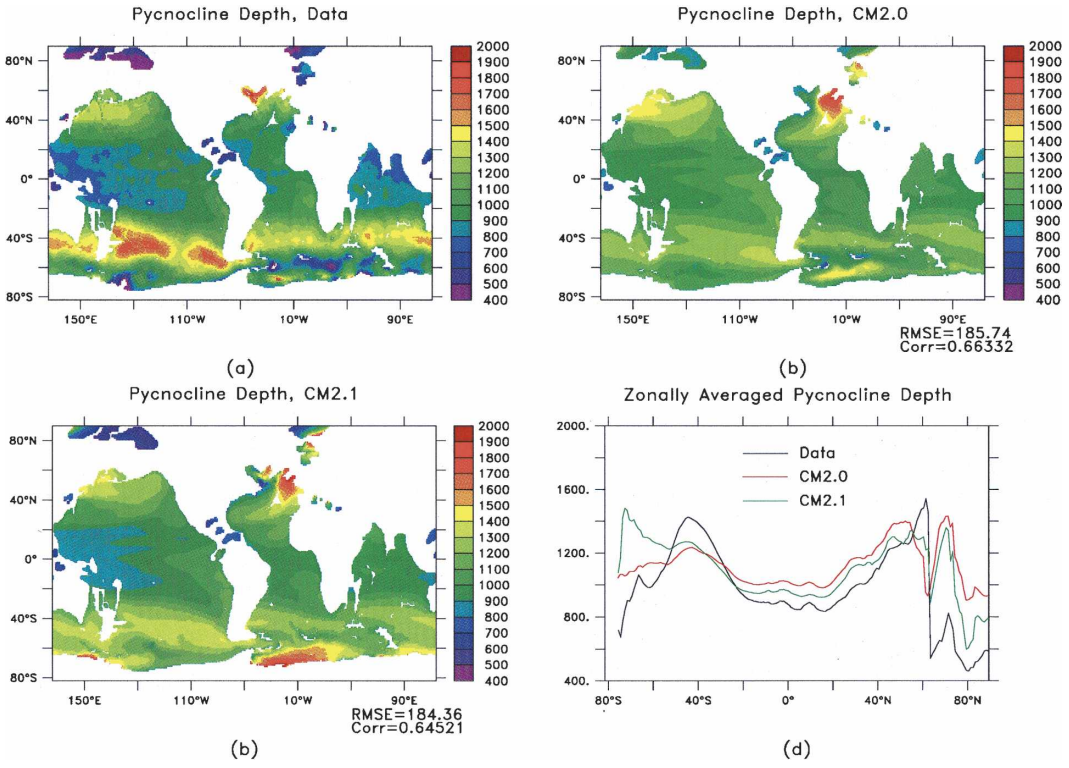

FIG. 4. Pycnocline depth in m as defined in Eq. (3) in (a) data, (b) CM2.0, and (c) CM2.1, and (d) zonally averaged in all three.

ciated with the North Atlantic Deep Water. In many models of ocean circulation, a significant fraction of the deep water upwells in tropical regions (Doney et al. 2004). In both CM2.0 and CM2.1 most of the water downwelling in the northern oceans travels all the way to the Southern Ocean—a signature that both the explicit and numerical diffusivities are low within the tropical pycnocline (Gnanadesikan et al. 2002). Note that there is some recirculation within the northern oceans in CM2.1, in part because there is more Labrador Seawater recirculating within the Atlantic. The CM2.1 model has a significantly stronger [21.9 versus 16.9 Sv ($1\ \text{Sv} \equiv 10^6\ \text{m}^3\ \text{s}^{-1}$)] overturning at 45°N. The overturning penetrates significantly deeper as well, with positive values seen down to 3000 m in CM2.1 as opposed to 2500 m in CM2.0.

Overturning in depth space tends to emphasize differences in deep circulations, which are quite important for the chemical and biological properties of the ocean. However, when it comes to heat transport, the surface wind-driven circulation plays a much more important role (Gnanadesikan et al. 2005; Bocaletti et al. 2005). The overturning in σ_2 space (Figs. 6b,d) shows that most of the watermass transformation crossing lines of constant density takes place in the Tropics, associated with equatorial upwelling, poleward flow in the mixed layer, and downwelling in somewhat surprisingly high latitudes (40° in both hemispheres, i.e., the mode water formation regions at the poleward edge of the subtropical gyres). The somewhat stronger equatorial winds in CM2.1 have two effects on this circulation. First they tend to intensify it, particularly in the Southern Hemisphere. However, as the increased upwelling results in a somewhat increased cold bias at the equator, the overturning does not extend as far into the light waters (resulting in the changes in Fig. 6f for densities between 1030 and 1032). The increase in the equator-to-pole circulation associated with enhanced Antarctic Intermediate Water formation in the Southern Ocean is seen in density space as well—but the increase in the deep Antarctic Bottom Water overturning is essentially invisible.

While no directly measured equivalent of the overturning exists, recent estimates have been made using geostrophic calculations from sections (Talley et al. 2003). These calculations show about 18 Sv of dense water formation in the Northern Atlantic, in relatively good agreement with the models. However, these calculations differ substantially from the models in the Southern Ocean, where the observational estimates have a massive formation of Antarctic Bottom Waters (21.8–27.3 Sv) while the models show a significant

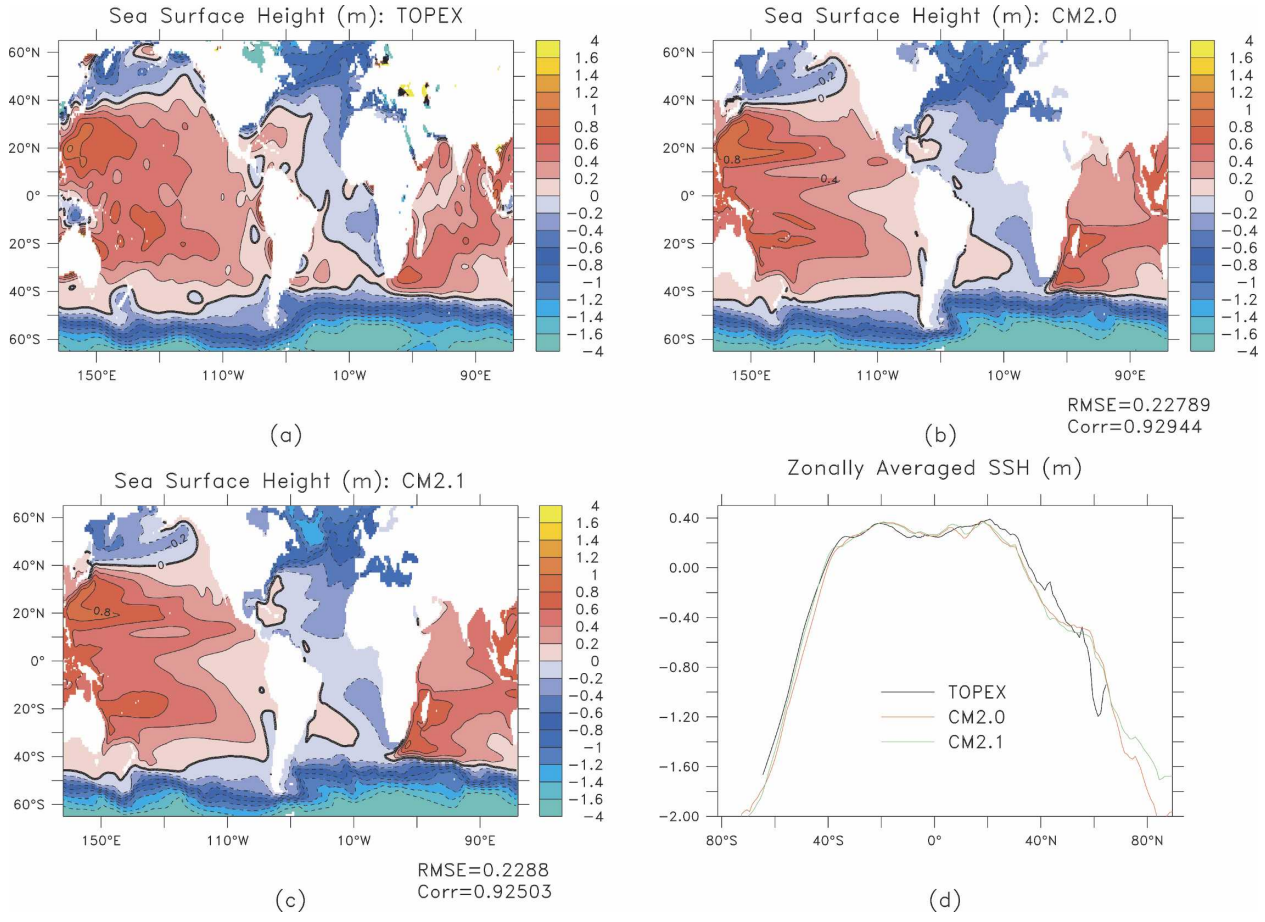

FIG. 5. Sea surface height in m for (a) data (TOPEX-Poseidon altimeter), (b) CM2.0, and (c) CM2.1, and (d) zonally averaged in all three.

transformation of deep waters to lighter waters. As in many models that have low diapycnal diffusion (Toggweiler and Samuels 1998; Gnanadesikan et al. 2002), our models show the Southern Ocean as a region of net lightening of surface waters. This picture is in agreement with the observational picture put forth by Speer et al. (2000), higher-resolution models (Hallberg and Gnanadesikan 2005, manuscript submitted to *J. Phys. Oceanogr.*, hereafter HAGN), and previously published coupled models (Doney et al. 1998). HAGN suggest that the difference between these observational syntheses based on hydrography and the numerical models may lie in the neglect of the effects of mesoscale eddies and the strong interaction between the flow and topography. It is also possible that long time-scale variability may be important.

Additionally, transports have been measured at a large number of locations in the global ocean. Some of these are shown in Table 1, compared with the model output. In general, the CM2.1 lies closer to the observed values than does CM2.0. Some of this is because of a stronger overturning in the North Atlantic, which results in a Deep Western Boundary Current and Florida Current closer to observations. Both models have too little export of Antarctic Bottom Water into the North Pacific, as seen by the low values in the Samoa Passage. The Indonesian throughflow and Kuroshio flows are on the high side as is the (relatively poorly constrained) Equatorial Undercurrent. The Antarctic Circumpolar Current (ACC) lies close to the higher observational estimates (widely accepted in the community) in CM2.1.

Ideal age (the age since water was last at the surface) is one way of looking at differences in ventilation. Figure 7 presents the ideal age 67.5 yr into the two simulations at depths of 800 and 2500 m. The results are compared with an age computed from CFC-12 data (Willey et al. 2004), defined as the year in which water with the observed partial pressure of CFC-12 would have been in equilibrium with the atmosphere. Since CFC-12 emissions began around 1930, these ages are at most 70 yr. Since ideal age in the model is initialized to

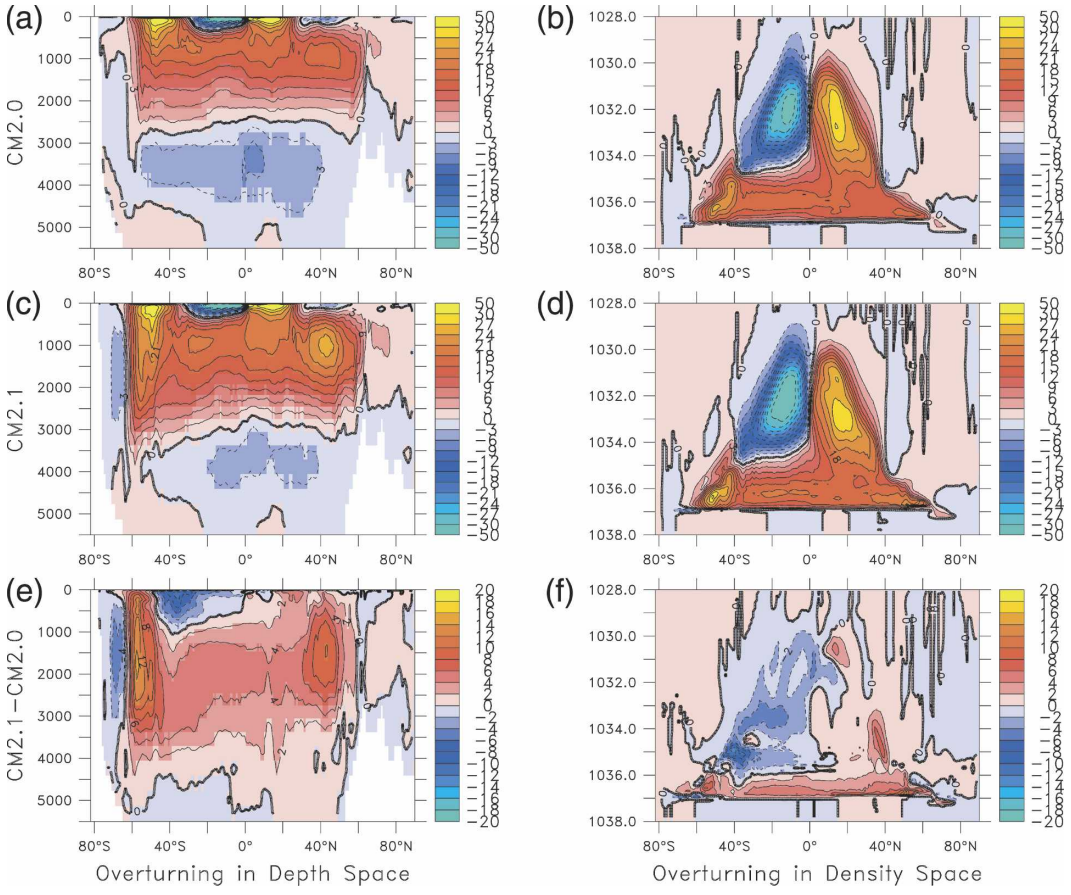

FIG. 6. Global overturning streamfunction (Sv) in (a) CM2.0 in depth space, (b) CM2.0 in potential density (referenced to 2000 m) space, (c) CM2.1 in depth space, (d) CM2.1 in potential density space, (e) CM2.1–CM2.0 in depth space, and (f) CM2.1–CM2.0 in density space.

zero, results are most comparable from years 65 to 70 in the model integrations. It should be noted that the CFC age will tend to underestimate the ideal age in regions where the mixed layers are very deep and the water injected into the ocean interior is not in equilibrium with the atmosphere. Additionally, in regions where concentrations are very low, individual measurements may be susceptible to contamination (also leading to CFC ages, which will be younger than ideal ages). When comparing the ideal age from the models to data, one should thus focus on the broad-scale patterns (in particular to location of strongly and weakly ventilated regions) rather than the exact numbers.

At 800 m, the data show ventilation occurring in the Labrador Sea, a band of high ventilation in the Southern Ocean in the latitudes of the Circumpolar Current, a band of weakly ventilated water to the south (corresponding to upwelling Circumpolar Deep Water), and ventilation around the Antarctic continent. There is also a clear signal at this depth of ventilation in the North Pacific and a weak (though clear) signal of ventilation from the Red Sea. The boundaries of the poorly ventilated areas in the tropical regions show up as waters older than 45 yr old. These "shadow zones" have long been known to be regions of low oxygen and are not directly ventilated from the surface because their potential vorticity is too low to connect with thick mixed layers in the midlatitudes (Luyten et al. 1983). At 2500 m the signal is significantly different. There are two main regions of ventilation, the North Atlantic and around the Southern Ocean. Signals from the Weddell and Ross Seas can be distinguished.

CM2.0 presents a picture that is qualitatively similar at 800 m, but quite different at 2500 m. The model represents most of the gross-scale features of the ventilation with signals from the North Atlantic, Southern Ocean mode and intermediate waters, and North Pacific mode water. The boundaries between recently ventilated waters and older waters in the shadow zones are well captured. However, there is no ventilation around the Antarctic boundary. This is even more clearly seen at 2500 m, where the North Atlantic Deep

TABLE 1. Transports at key locations in the model. North Atlantic Deep Water (NADW) formation is from Talley et al. (2003). High observed value of ACC at Drake Passage is from Cunningham et al. (2003); lower value is from Orsi et al. (1995). Higher value of ACC transport is likely to be more accurate as it includes an (observed) barotropic component. Indonesian throughflow is from Gordon et al. (2003), Florida Current from Leaman et al. (1987), and Kuroshio from Lee et al. (2001), using current meters off of Taiwan and consensus estimates of flow east of the Ryukyu Islands (which are not resolved in the models). Bering Strait observations are from Roach et al. (1995). High value for Equatorial Undercurrent at 155°W is ADCP data from the Tahiti Shuttle Experiment (Lukas and Firing 1984); low value is from the inverse model of Sloyan et al. (2003). Samoa Passage transport is defined as net transport of water less than 1.2°C (Johnson et al. 1994; Freeland 2001). The Atlantic Deep Western Boundary Current at 5°S is taken from Rhein et al. (1995).

Current name	Observed (Sv)	CM2.0 (Sv)	CM2.1 (Sv)
NADW formation	18	16.9	21.3
ACC (Drake Passage)	97/134	116	132
Indonesian Throughflow	≈10	15.6	13.9
Florida Current	28.7–34.7	19.0	26.8
Kuroshio (24°N)	29–40	48.3	41.7
Bering Strait	0.83	0.60	0.87
Equatorial Undercurrent (155°W)	24.3–35.7	38.0	34.6
Atlantic DWBC (5°S)	19.6–33.8	19.6	21.7
Samoa Passage	3.3–8.4	−0.2	1.4

Water represents the only signal of ventilation. Such a lack of ventilation has important implications for the carbon cycle (Toggweiler et al. 2003; Marinov 2004), implying that the venting of deep waters rich in carbon dioxide is essentially capped off by stratification in the Southern Ocean.

Many, though by no means all, of the model–data differences are less pronounced in CM2.1. At 800 m, there is a clear banded structure in the Southern Hemisphere, (particularly in the Atlantic sector) where one can distinguish young waters near the continent; older, upwelling Circumpolar Deep Water away from the continent; and young intermediate waters farther to the north. The ventilation around the continent penetrates to significant depths, as seen in the ideal age at 2500 m. Analysis of CM2.0 and CM2.1 at subsequent times shows that this difference persists. Although CM2.0 does occasionally ventilate the deep waters of the Southern Ocean, such ventilation is much weaker than in CM2.1.

The age structure in CM2.1 also exhibits other improvements relative to CM2.0. For example, the North Pacific waters are clearly younger at 800 m in CM2.1. In the North Atlantic there is a clear signal of convection in the Labrador Sea, implications of which are discussed in more depth in the companion paper by Stouffer et al. (2006). However, there are certain features (excessive ventilation in the northeast Atlantic at 800 m; lack of ventilation in the northwest Indian Ocean) that do not change between the models.

4. Regional diagnostics

a. Southern Hemisphere

Since it has already been shown that the largest differences in temperature and salinity errors between the models occur in the Southern Hemisphere, we begin our analysis in this region. One of the striking differences between CM2.0 and CM2.1 is the difference in the rms temperature error seen in Figs. 3a and 3b. Interestingly, the largest errors in CM2.0 do not show up at the surface, but rather reach their maximum at a depth of around 500 m. Figure 8 shows a close-up of the temperature error and circulation at 500 m in the two models. Observations (Ridgway and Dunn 2003) and high-resolution numerical models (Tilburg et al. 2001) suggest that the real East Australia Current splits at a latitude of 30°S with the Tasman front striking off to the east and the East Australia Current extension (EACE) continuing to the south. In CM2.0, the East Australia Current extension essentially feeds all its transport into the Tasman front, carrying warm subtropical water deep into the South Central Pacific. In CM2.1 by contrast the East Australia current continues to the south and feeds the Flinders Current south of Tasmania.

The difference between the two circulations can largely be explained in terms of the wind stress curl. In CM2.0 strong positive wind stress curl is only found northward of 42°–44°S in the South Pacific, so that the bulk of the subtropical gyre lies to the north of New Zealand. In CM2.1 the wind stress curl between New Zealand and South America remains positive down to 55°S, so that all of New Zealand lies within the Subtropical Gyre. RGT discuss this issue in more detail.

The big improvement in rms salinity error between CM2.0 and CM2.1 is seen in the south Atlantic Ocean. The source of the error is the position of the subtropical front (STF). Figure 9 shows the location of the subtropical front [defined, as in Orsi et al. (1995) as where the 34.9-isohaline surface is found at a depth of 100 m]. In the observations, the subtropical front crosses the south Atlantic and south Indian Oceans between the latitudes of 36° and 40°S, well to the south of the Cape of Good Hope and the main body of the Australian continent. In CM2.0, the STF deviates far to the north in both the Atlantic and Indian Oceans. The errors are most prominent in the Atlantic, where the STF reaches a latitude of 22°S. In CM2.1, the situation is much improved, with the STF retreating southward by almost

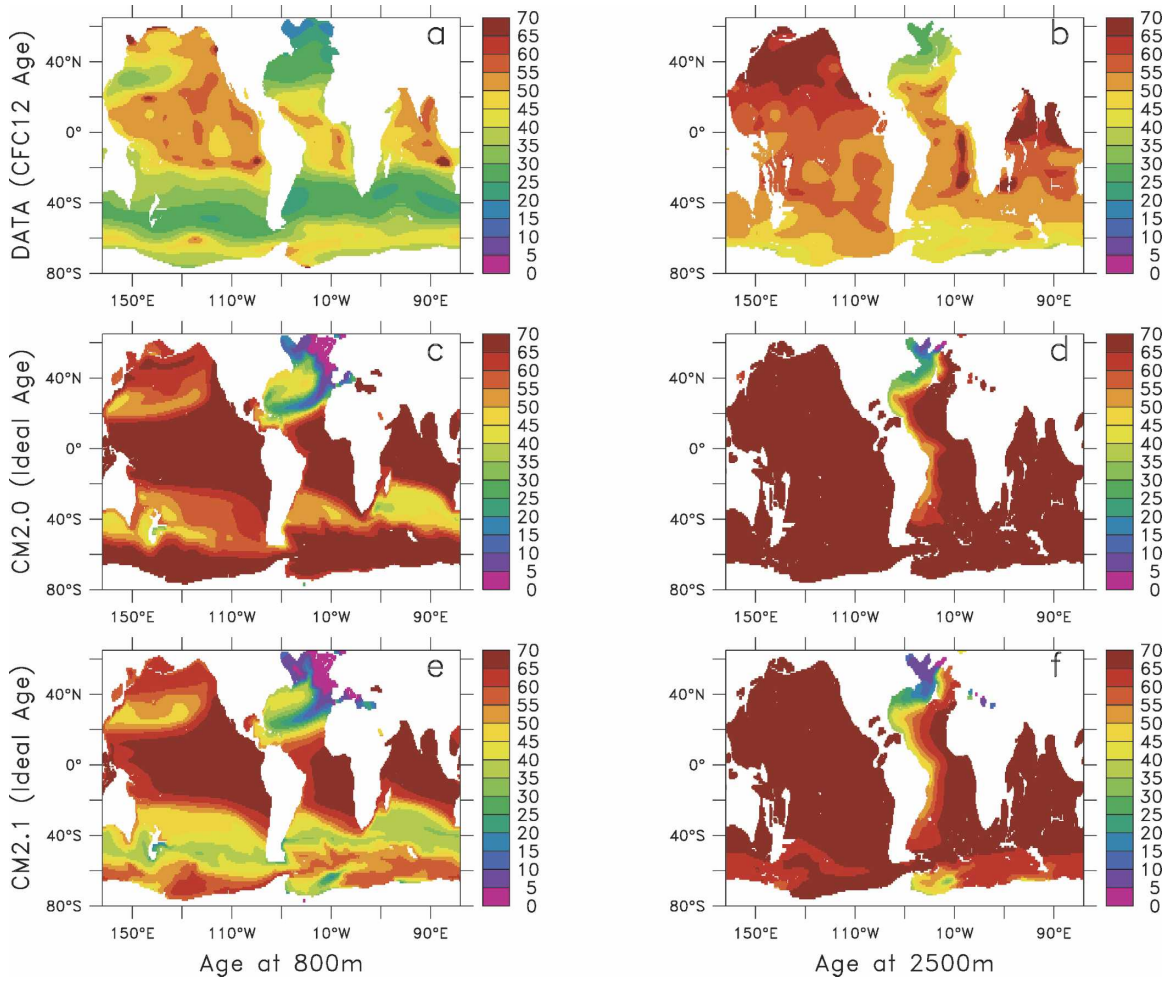

FIG. 7. Age in years: CFC-12 age [from the dataset of Willey et al. (2004)] at (a) 800 and (b) 2500 m. Ideal age at (c) 800 and (d) 2500 m for CM2.0. Ideal age at (e) 800 and (f) 2500 m for CM2.1.

10° in the southeast Atlantic. Significant errors remain in the Pacific, however, in that the STF still intersects the Australian continent, so that the mode waters formed to the south of Australia are still too fresh.

There are several possible sources for the errors in the simulation of the STF in CM2.1. Off of Australia, one possibility is related to excessive precipitation in the South Pacific associated with the southern branch of the ITCZ, resulting in a gyre that is insufficiently salty. This fresh signal is then propagated by the East Australia Current extension into the mode water formation regions to the south of Australia. A second possible source of error is that the Indonesian throughflow transport is too high, so that water that should be going to the south of Australia is diverted around to the north. Off of Africa, a possible source of error is that even a 1° model does not represent the Agulhas eddies that bring salty water from the Indian Ocean into the Atlantic. Examination of simulations conducted as part of the Modeling Eddies in the Southern Ocean (MESO) Project (HAGN) show that in a 1° model that does not resolve ocean eddies the STF does extend farther to the north than in finer-resolution models that capture the formation of coherent Agulhas eddies.

b. North Atlantic

The second major source of rms error in both temperature and salinity is the North Atlantic Ocean. Figure 10a shows the potential density and the salinity at 35°N in the North Atlantic. A standard subtropical gyre structure is seen, with isopycnals tending to shallow toward the east. The isohalines tend to follow the density in the upper part of the water column but deviate sharply in the east below about 800 m, where the influence of the Mediterranean outflow is seen. The hydrographic structure in CM2.0 differs significantly from the data. The difference shows up in the intermediate water layer between $\sigma(\theta) = 27.0$ and 27.5. This layer is sub-

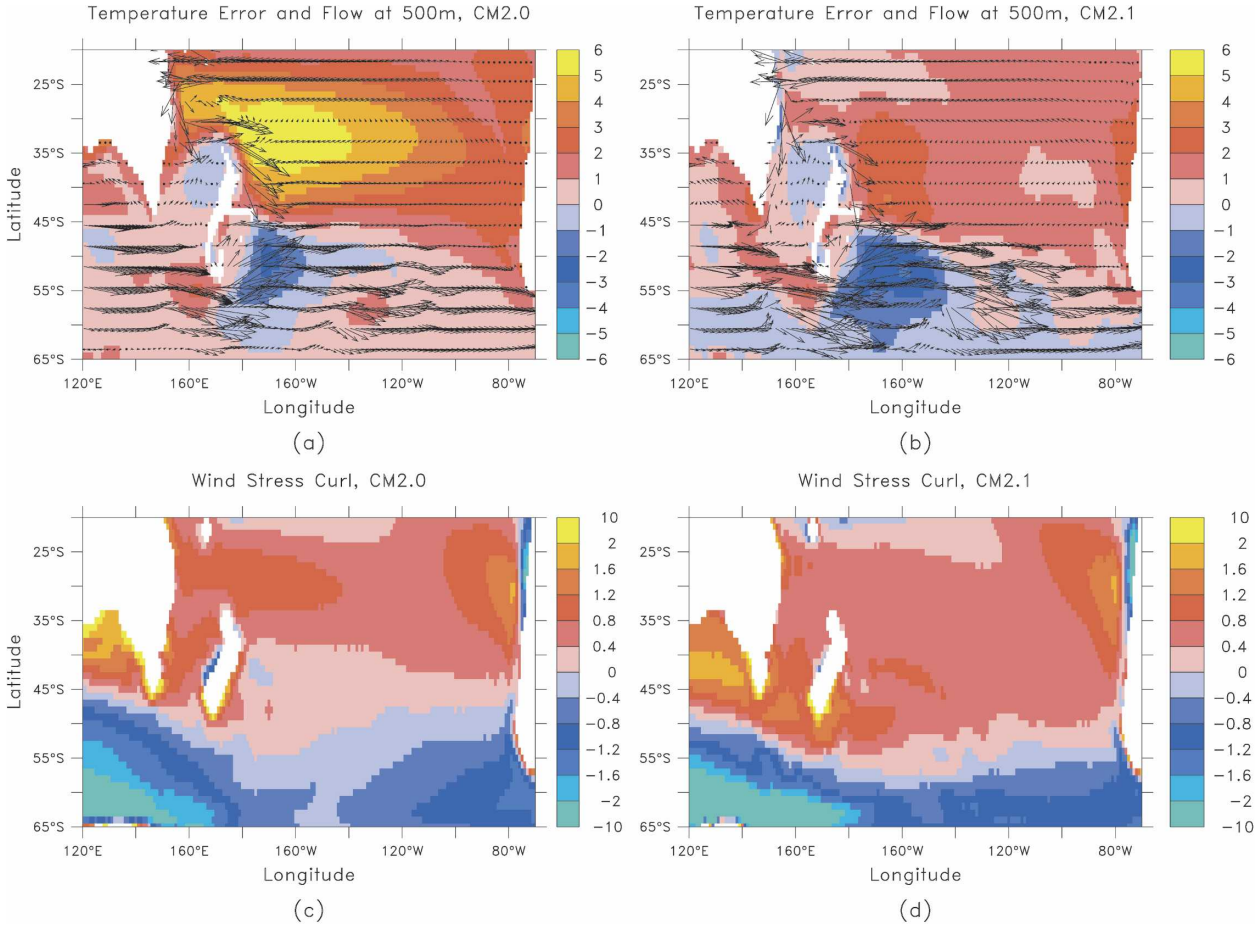

FIG. 8. Preliminary analysis of the southern Pacific temperature bias. (a) Temperature bias in °C relative to observations at 500 m in CM2.0 with transports overlaid. Note the large transport in the Tasman front and the nonexistence of the EACE. (b) Same as in (a), but for CM2.1. Note that there is now a much weaker eastward transport to the north of New Zealand and a stronger EACE. (c) Wind stress curl (in units of 10^{-7} Pa m^{-1}) in CM2.0. (d) Wind stress curl in CM2.1.

stantially thicker than observed in the eastern part of the basin. In CM2.1, the bias is reduced, but this layer is still far too thick.

Analyses of the observed structure of the intermediate water layer (Fig. 10b) show that it has a maximum thickness in the Tropics and northeastern Atlantic, and a minimum thickness in the center of the gyre recirculation in the west. A trough of lower thickness crosses the basin, reaching the eastern boundary. This trough is associated with a layer potential vorticity maximum that separates the northern waters from the tropical waters. In CM2.0 (Fig. 10d) this trough in PV is not present. Instead, the intermediate water layer is extremely deep in the northeast Atlantic, and the low PV associated with this water forms a plume that extends into the Tropics. The layer thickness and PV structure in CM2.1 is closer to the observations, but the connection between the northeast Atlantic and the Tropics remains.

Why are the northeast Atlantic and Tropics not connected along this isopycnal in the real world? Three possible reasons are explored in Fig. 11. The first relates to the details of surface boundary conditions. In CM2.0, low-salinity water caps off the Labrador Sea, forcing convection to occur farther to the east. This convection is so deep that the low PV water it creates is able to connect to the Tropics through the gyre interior, rather than along the boundary. Huang and Pedlosky (2000) describe a mechanism of this sort in a simple 2-1/2-layer model. In CM2.1, there is a shift in convection into the Labrador Sea (as seen by the salinity in Fig. 11 and the age in Fig. 7e), and the interior pathway is significantly reduced. However, this does not lead to a reduction in the salinity error. In fact the salinity errors in the intermediate water layer actually increase.

A more subtle explanation would involve the details of the wind stress curl. The PV contours in the intermediate water layer in observations originate to the

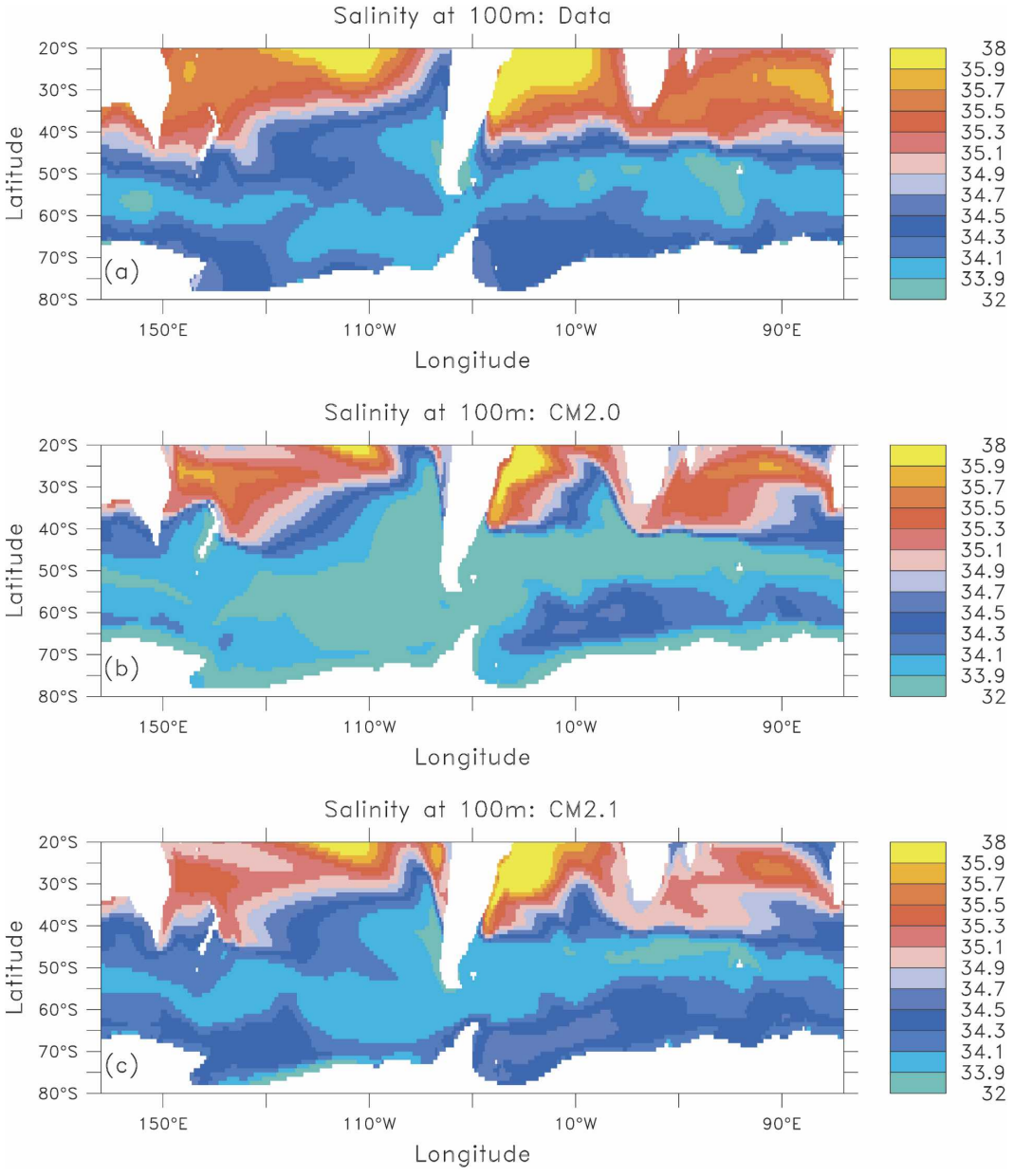

FIG. 9. The subtropical front in the Southern Ocean. (a) Salinity in PSU at 100 m in data [color change is location of subtropical front as defined in Orsi et al. (1995)]. (b), (c) Salinity in PSU in CM2.0 and CM2.1, respectively.

north of the line of zero wind stress curl, within the subpolar gyre. That this can happen is in part due to the fact that the zero wind stress curl line slants across the basin from the southwest to the northeast. Since wind-forced layers tend to become thinner moving to the west in regions with positive curl and thicker in regions of negative curl, the fact that the region of positive curl extends farther to the south in the models means that the wind-driven layer in the basin interior will tend to be thinner than it should be in the models. In both models the intermediate water layer is too thin off of Iceland, and hence cannot create a PV structure of the form seen in Fig. 11a.

A final potential explanation is the details of the Mediterranean outflow. In the real world, the Mediterranean outflow entrains water from the intermediate water layer as it descends the slope but largely lies below this layer. Özgökmen et al. (2001) note that the dynamical effect of this will be to create a trough of low thickness in the intermediate water layer, which will act to interrupt the equatorward flow of colder northern water in the gyre interior. In both models, however, the

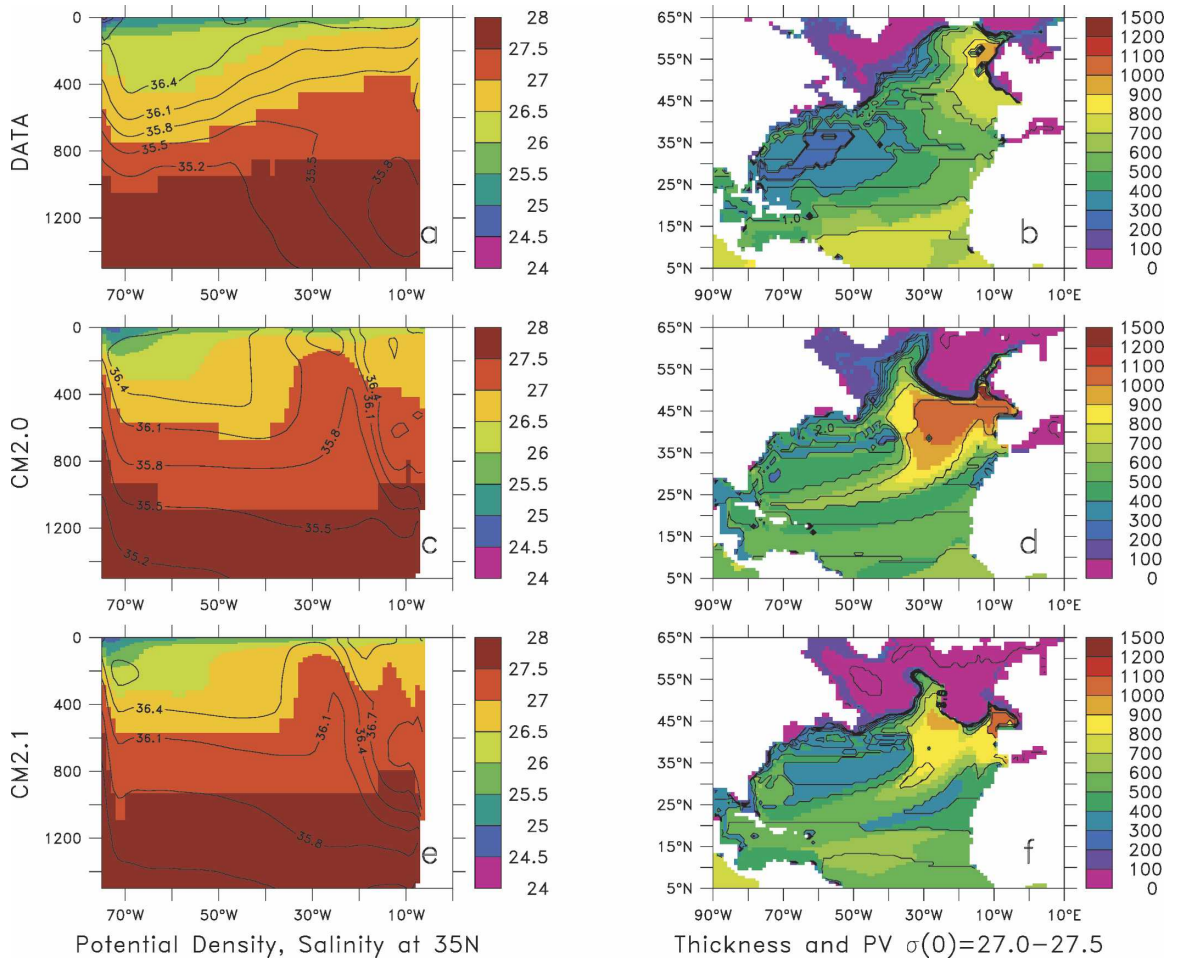

FIG. 10. Structure of bias in the Atlantic Ocean. (a) Upper-ocean potential density (kg m^{-3}) and salinity in *World Ocean Atlas 2001*. (b) Depth of intermediate water layer [$\sigma(0)$ between 27.0 and 27.5] in m and layer PV (f/h in 10^{-7} m^{-1} s^{-1}) in data. (c) Same as in (a), but for CM2.0. (d) Same as in (b), but for CM2.0. (e) Same as in (a), but for CM2.1 (f) Same as in (b), but for CM2.1.

Mediterranean water is mixed into the intermediate water layer (hence the large errors in salinity) instead of largely lying below it. It is thus possible that the thinning due to the Mediterranean beta plume is underestimated.

c. North Pacific

The North Pacific is another region where substantial errors are seen in the hydrography in CM2.0, with significant improvements in CM2.1. This improvement largely arises from changes in the shallow wind-driven circulation. Figure 12 shows the temperature error and wind stress curl in CM2.0 and CM2.1 between 0 and 200 m. In CM2.0, a very strong tongue of excessively cold water extends over the North Pacific. This appears to be associated with the fact that extremely cold surface water (which is also quite fresh) is found off of Hokkaido. This water then becomes entrained in the subtropical gyre, severely distorting the temperature structure. The line of zero wind stress curl penetrates a long way to the south in CM2.1 and has a much steeper northward drift across the Pacific than is found in the real world, where it is essentially zonal. This distortion in the wind stress curl is implicated in allowing subpolar waters to penetrate too far south and to become entrained in the subtropical gyre.

In CM2.1, by contrast, the line of zero wind stress curl is more zonal and the Kuroshio penetrates farther to the north. This warms the North Pacific, actually increasing the errors near Japan where the Kuroshio overshoots. The net effect is to reduce the dispersion of overly cold waters into the subtropical thermocline.

d. Northern Indian

A final area that shows significant hydrographic errors is the northern Indian Ocean. These errors are

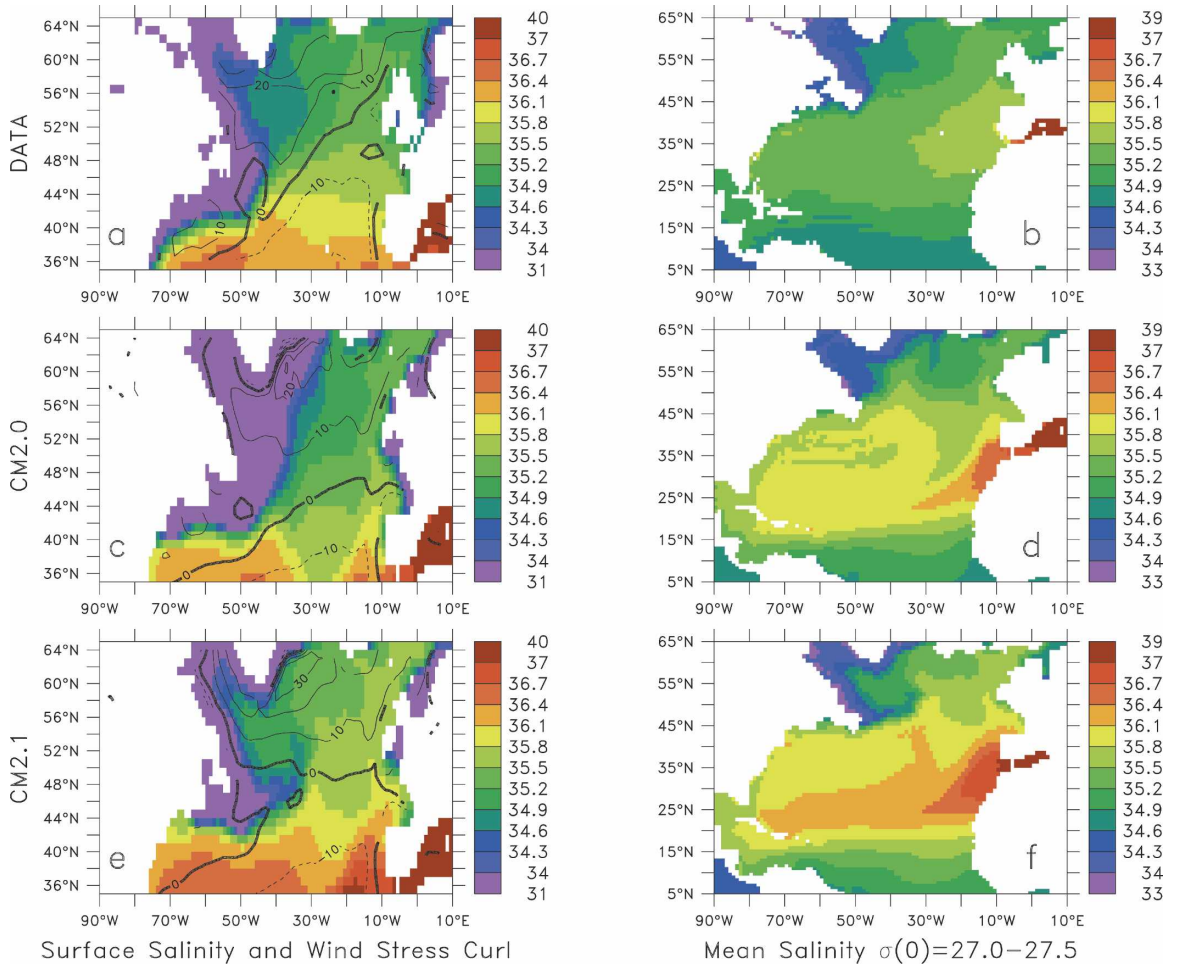

FIG. 11. Structure of bias in the Atlantic Ocean. (a) Surface salinity in *World Ocean Atlas 2001* in PSU and wind stress curl (10^7 Pa m^{-1}) from European Centre for Medium-Range Weather Forecasts (ECMWF) reanalysis. (b) Mean salinity (PSU) of intermediate water layer [$\sigma(0)$ between 27.0 and 27.5] in *World Ocean Atlas*. Surface salinity and wind stress curl in (c) CM2.0 and (e) CM2.1. Mean salinity (PSU) in intermediate water layer in (d) CM2.0 and (f) CM2.1.

clearly associated with the Red Sea outflow. Figure 13 shows salinities across the northern Indian Ocean at 13°N. The data show a pattern with salty water at the surface, relatively fresh waters immediately below, and a salty plume from the Red Sea centered at a depth of 600 m.

In both CM2.0 and CM2.1, the salinity structure is almost completely different. The freshest water is found at the surface, a layer of salty water is found below that, and the Red Sea plume is too shallow. While the error in CM2.1 is smaller than in CM2.0, examination of the salinity structure shows that the upper part of the water column is actually fresher than in CM2.0. This enhanced fresh bias at the surface may play an important role in reducing the salt bias at depth.

It is interesting that both the Red Sea and Mediterranean overflows appear to produce error patterns in which the overflow fails to descend to the appropriate depth while entraining ambient water. There are two possible reasons for this. The first is the inability of models to represent the thin boundary layer, as discussed by Winton et al. (1998), resulting in too much mixing between the dense water and light surface water. The second is that the overflow is represented as a mixing between the marginal sea and the open ocean rather than as an injection of mass along an isopycnal, so that the marginal sea properties are lost before they can even begin to descend the slope. Analysis of which of these processes is most important will be the subject of a future paper. It should be noted that these errors do not appear to produce large errors in the coupled variability of the tropical Indian Ocean. SVR show that

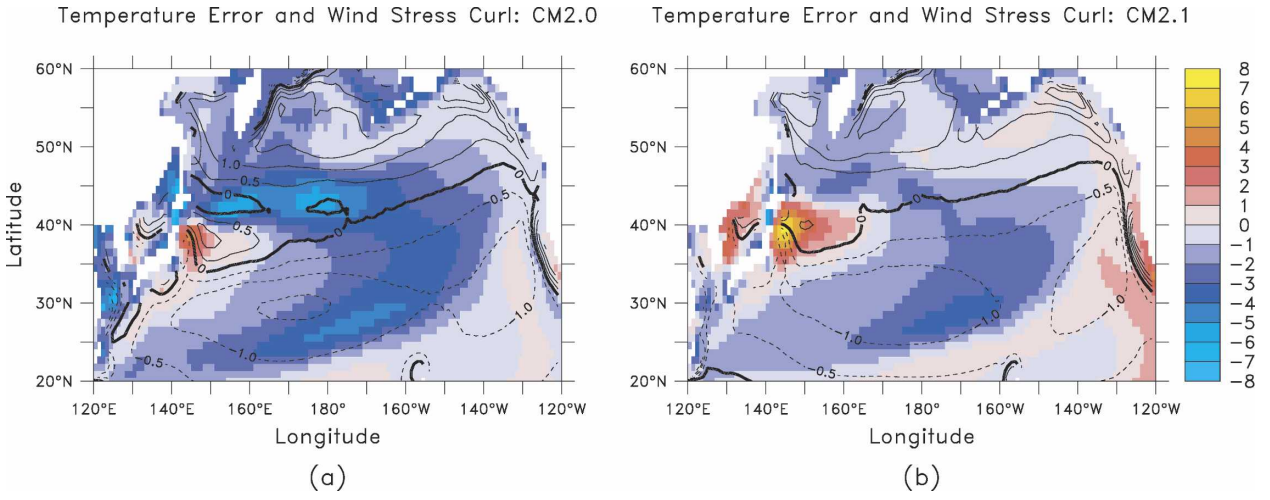

FIG. 12. Temperature errors in the northwest Pacific: temperature error in °C and wind stress curl in 10^{-7} Pa m^{-1} for (a) CM2.0 and (b) CM2.1.

the model captures both pattern and magnitude of the major modes of variability in sea surface temperature within this basin.

e. *Arctic*

Of all the parts of the ocean, the representation of the Arctic has changed the most relative to previous models, with the inclusion of a tripolar grid and concommitant removal of polar filtering in the ocean. As a result, the model is now able to resolve flows through the Arctic. Figure 14 shows the surface ice thickness and ice velocity in CM2.0 and CM2.1. Colony and Thorndike (1984) showed that the ice drift in the Arctic tends to follow contours of sea level pressure. As a result, the pattern of ice drift is anticyclonic about a center on the Bering Strait side of the Arctic. A significant outflow of ice occurs through Fram Strait to the northeast of Greenland. This qualitative pattern is seen in both models. The location of the center of the anticyclone is essentially correct.

Details of the pattern, however, are not correct. In particular the center of the anticyclonic drift extends almost all the way to the pole in CM2.0. Analysis shows that the main reason for this is errors in the sea level pressure distribution in the Arctic. In observations, the Icelandic low extends northeastward, into the Arctic to the north of Norway and into the White Sea. The polar high in sea level pressure is actually quite weak. In CM2.0 there is a very strong polar high (+6 mb in the annual mean and up to 10 mb in December and January

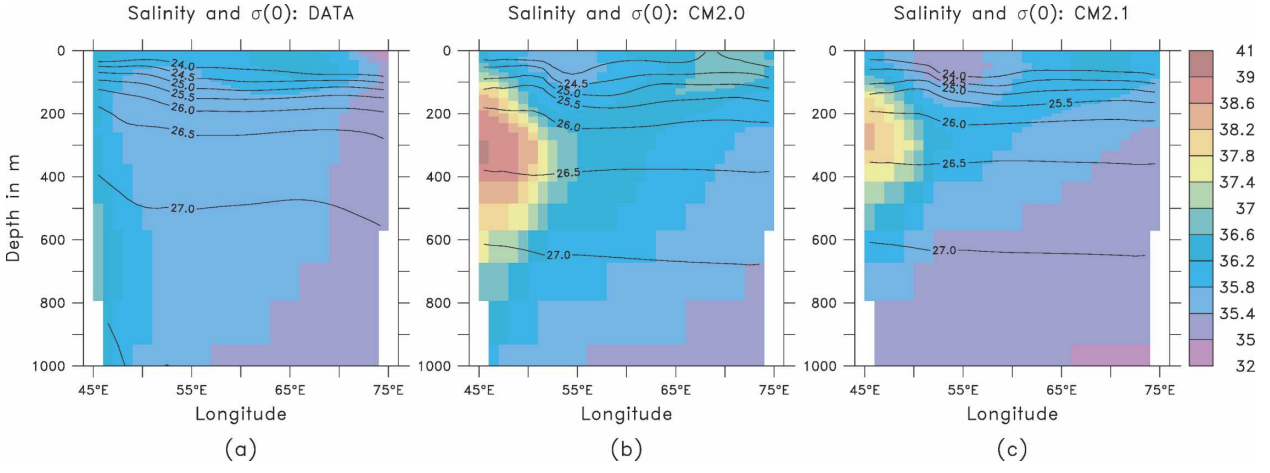

FIG. 13. Salinity in PSU (colors) and density in kg m^{-3} (contours) structure in the northwest Indian Ocean at a latitude of 13°N: (a) data, (b) CM2.0, and (c) CM2.1.

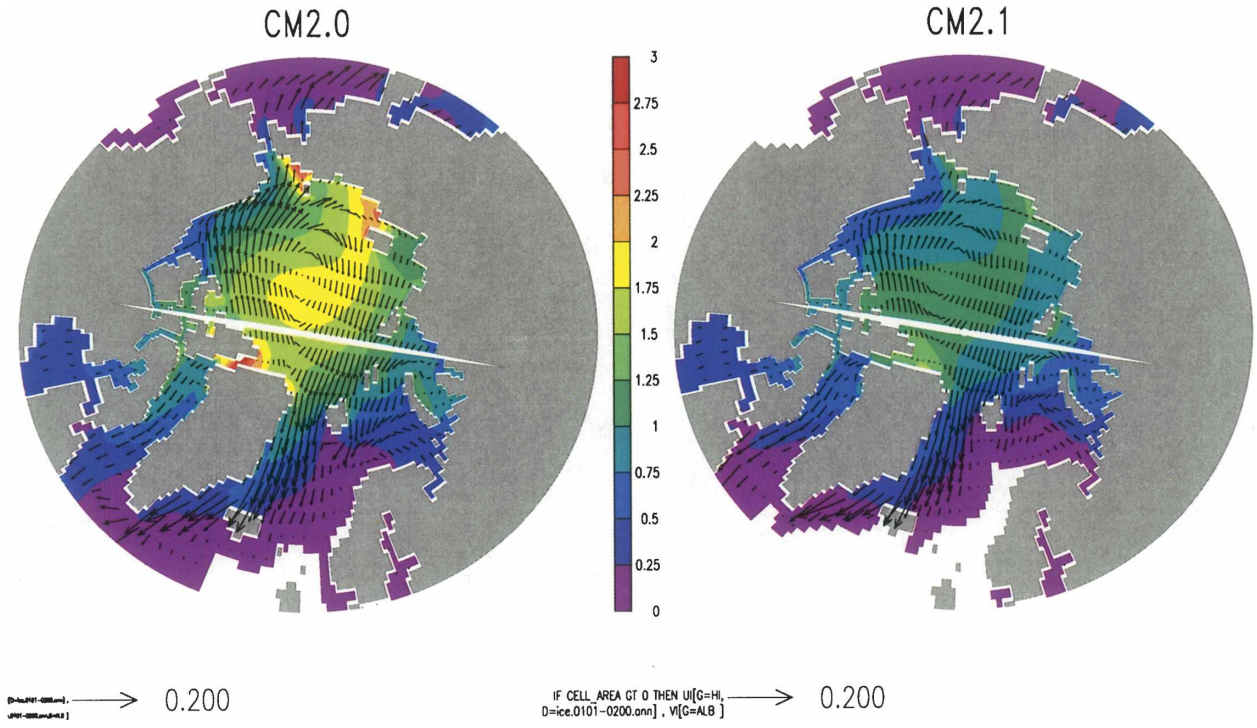

FIG. 14. Ice thickness (in m, colors) and drift (in m s^{-1}, vectors) in the Arctic: (a) CM2.0 and (b) CM2.1.

relative to observations). In CM2.1, the bias in the polar high is reduced by about 50%. Indications of this difference can be seen in the drift patterns. In CM2.1, the drifts are much weaker in the Canadian Arctic, and the center of the drift is clearly displaced toward the Bering Strait. However, ice drift speeds are still higher than in observations [3–4 cm s^{-1} versus 1–3 in the observations of Barry et al. (1993)].

One reason for excessively fast ice drift is that the ice is too thin. Observations of annual ice thickness near the North Pole have been observed from submarines to be around 4 m (Rothrock et al., 2003), while both models predict values less than 2 m. Analysis of the annual cycle of sea ice suggests that the onset and completion of the snowmelt season occur earlier than in observations, resulting in too low an albedo during the time of highest radiation. Sensitivity studies to understand this bias are ongoing.

Signatures of the biases in sea level pressure can also be seen deeper in the water column. As noted by Rudels et al. (1994), the circulation in the deep basins in the Arctic is cyclonic, the reverse of the anticyclonc circulation in the surface layer. This cyclonic circulation brings Atlantic water via the Norwegian Coastal Current and along the coast of Spitsbergen. At this point, the Atlantic Water is entrained by the anticyclonic circulation and moves along the Siberian Arctic shelf. Figure 15 shows the observed temperature and potential density along a section in the western Arctic, corresponding to the models' 85°N coordinate line in the western Arctic. The Atlantic water can be seen as a warm tongue in the western part of the section. By contrast, in CM2.0, the circulation is anticyclonic to great depth, and the warmest water is found along the North American side of the basin rather than along the Siberian side. While the temperature structure is somewhat improved in CM2.1 (Fig. 15c), the circulation now involves a cyclonic circulation along the Siberian side of the basin with an anticyclonic circulation along the Canadian side of the basin.

5. Discussion

We now turn to the question of whether our analysis of the error patterns seen in the CM2.0 and CM2.1 models tells us anything important about the climate system. The two models have different atmospheres, which produce different air–sea fluxes, particular of momentum (Delworth et al. 2006, their Fig. 1) as well as different lateral mixing schemes for momentum and tracers. In Table 2 we present a number of indices of model error in CM2.0, CM2.1, and two developmental runs using the CM2.1 atmosphere in which the lateral mixing of tracers and momentum were changed sepa-

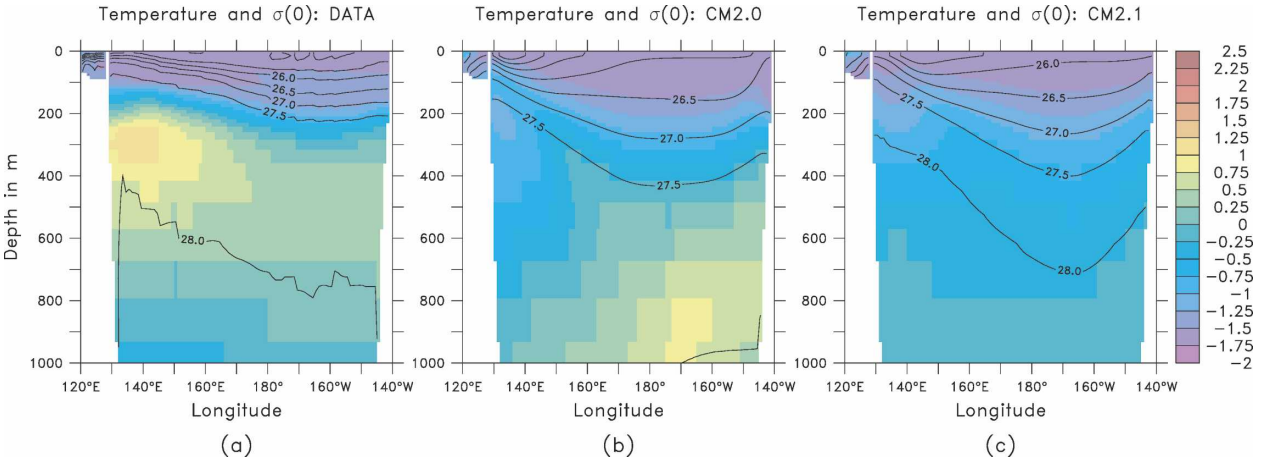

FIG. 15. Temperature (°C, colors) and density (kg m^{-3}, contours) structure in the western Arctic along the model latitude of 85°N: (a) data, (b) CM2.0, and (c) CM2.1.

rately. This enables us to gain some insight about key parts of the ocean circulation, as well as the parameter dependence of coupled models.

One of the major improvements in CM2.1 relative to CM2.0 is the circulation and temperature structure of the Southern Ocean. This appears to be primarily due to the changes in the atmosphere. All three models run with the finite-volume atmosphere (used in CM2.1) have poleward-shifted winds and concommitant increase in deep ventilation in the Southern Ocean (Fig. 7 and second row of Table 2); reduction in the South Pacific temperature error (Fig. 8 and third row of Table 2); poleward shift of the subtropical front, especially in the Atlantic sector (Fig. 9 and fourth row of Table 2);

TABLE 2. Comparison of changes between the CM2.0 model (second column), CM2.1 model (right column), and two intermediate models. In the first case (third column) the atmosphere represents the primary change. In the second case (fourth column), the lateral diffusivity scheme has been changed as well. Comparing the second and third columns allows evaluation of the impact of the atmospheric circulation, comparing the third and fourth allows evaluation of the impact of the isopycnal diffusivity, and comparing the fourth and rightmost columns allows evaluation of the impact of extratropical background viscosity. Fields computed over years 21–60 (as well as ideal age deficit) are shown in regular type; fields computed from years 101–200 are shown in italics. The fields compared are global rms temperature error (cf. Fig. 3), age anomaly in the Southern Ocean at 60 yr into the coupled simulation (age−60.5, giving a measure of the degree to which young waters are being added to this depth; compare with Fig. 7), rms temperature error in the SW Pacific (cf. Fig. 8), error in the latitude of the subtropical front (southeast Atlantic; cf. Fig. 9), transport of the ACC, Florida Current, and North Atlantic Overturning (cf. Table 1), surface salinity error in the Labrador Sea (50°–60°N, 50°–40°W), salinity error near the mouth of the Red Sea (13°N, 45°–50°E, 200–500 m), mean sea ice concentration in an ice-free part of the northwest Pacific, inflow of water in the western basin of the Arctic along the model latitude of 85°N (300–600 m), and temperature bias in the north-central Pacific.

	CM2.0	CM2.1 atm CM2.0 A_I CM2.0 viscosity	CM2.1 atm CM2.1 A_I CM2.0 viscosity	CM2.1 atm CM2.1 A_I CM2.1 viscosity
Rms temperature error; global (0–1500 m) °C	1.14/*1.48*	1.09	1.04	1.02/*1.28*
Age anomaly at 2500 m; 80°–60°S (yr)	−0.1	−7.1	−4.1	−4.5
Rms temperature error (SW Pacific 0–1500 m) °C	1.35/*1.85*	0.79	0.79	0.75/*1.00*
Error in latitude of subtropical front (Atlantic sector; degrees)	−7.6/*−7.8*	−3.4	−3.2	−3.2/*−4.5*
ACC transport at Drake Passage (95–135 Sv)	124/*111*	152	137	139/*132*
Florida Current transport (30 Sv)	19.6/*18.9*	17.5	16.7	26.4/*27.2*
North Atlantic overturning at 45°N (Sv)	18.4/*16.3*	18.6	17.8	21.7/*24.6*
Surface salinity error PSU (Labrador Sea)	−0.68/*1.52*	−1.00	−0.94	−0.12/*0.20*
Rms salinity error (0–1500 m; 0°–60°N; Atlantic)	0.46/*0.54*	0.46	0.43	0.41/*0.55*
Salinity error (PSU); Red Sea outflow (200–500 m)	2.29/*2.57*	1.90	1.49	1.36/*1.43*
Mean sea ice concentration; 40°–50°N, 150°–175°E	0.21/*0.19*	0.15	0.12	0.10/*0.06*
Western inflow; Arctic; 200–400 m (Sv)	−0.45/*−0.48*	−0.88	−0.46	−0.76/*−1.45*
Temperature bias in °C; north-central Pacific (0–200 m)	−3.19/*−2.84*	−1.52	−1.82	−2.12/*−1.67*

and increase in ACC transport (fifth row of Table 2). Both the age and ACC transport appear to have sensitivity not only to the winds, however, but to the lateral mixing of tracer and a somewhat weaker sensitivity to the lateral viscosity, with more ventilation being associated with a stronger ACC transport.

The viscosity also appears to have an impact on other currents. The most important of these is the Florida Current (sixth row of Table 2), which is less than 20 Sv for all of the runs with high extratropical isotropic viscosity. Only when a low value of extratropical viscosity is used does the transport rise to a more reasonable value of 26–27 Sv. A somewhat weaker sensitivity is found with respect to the North Atlantic overturning (seventh row of Table 2). This quantity drops over the first century of the CM2.0 integration relative to years 21–60 but does not do so in the finite-volume runs, and actually spins up to a higher value in the CM2.1 run (see Delworth et al. 2006, their Fig. 8). The increase in CM2.1 is related to the surface salinity in the northeast Atlantic (Fig. 11 and 8th row in Table 2), which is not improved by the change in the atmosphere or the isopycnal diffusion but is strongly affected by the viscosity. Analysis of the current structure (not shown) reveals that reducing the viscosity allows for a much stronger circulation in the Labrador Sea. The result is a more efficient export of the freshwater, which otherwise caps off the Labrador Sea and prevents convection. Improvements in the mean salinity error in the entire North Atlantic (9th row of Table 2) appear to be due to a combination of causes, as do the salinity errors associated with the Red Sea outflow (10th row of Table 2; compare with Fig. 13), the reduction of sea ice in the northwest Pacific Ocean (11th row of Table 2; compare with Fig. 14 in Delworth et al. 2006), and the degree to which there is actually an anticyclonic current at depth in the in Arctic (12th row of Table 2). In at least one measure of model fidelity, the upper-ocean temperature error in the North Pacific documented in Fig. 12 of this paper, the changes made in the ocean do not seem to have improved the situation, as the error actually increases as the diffusion and viscosity are changed (last row of Table 2). This illustrates the difficulty of constructing a model of this complexity. Even within a region where the changes to the ocean circulation improve the sea ice they do not necessarily improve the hydrography.

Taken together, these results point to the paramount importance of the wind stress distribution in determining the ocean circulation, since this is the flux field that changes most between the two classes of models. In individual regions, however, the details of the lateral mixing of tracer and momentum (the latter of which is poorly known) can have an important role. This has implications for whether climate changes in such regions can be robustly compared with observations.

6. Conclusions

When a model is referred to as "realistic," two different meanings are often assigned to the term. The first is that the model simulates large-scale distributions of properties such as temperature, salinity, and tracers with relatively low errors. The second is that the model includes realistic representations of processes known to act in the real world, so that it is not getting the right answer for the wrong reasons, that is, canceling numerical errors. We would argue that the CM2 series meets both criteria in many comparisons with observations, though it should be noted that the simulations have only been run out for a few centuries.

The CM2 ocean models we have presented here differ substantially from previous versions of the GFDL coupled models. New numerical developments include a tripolar grid, elimination of polar filtering, higher resolution in both the horizontal and vertical, better representation of topography, inclusion of an explicit free surface, inclusion of an explicit mixed-layer model, improved tracer advection, inclusion of the effects of advective flows introduced by mesoscale eddies, a representation of bottom boundary layers, and new lateral mixing schemes for momentum. Additionally, the vertical diffusion of tracers in the tropical pycnocline is far lower than in previous models. The ocean code is also run under very different conditions than previous models, without flux adjustments of any kind.

The resulting simulations of the ocean reproduce most of the major features of the ocean circulation, capturing the large-scale overturning, gyres and boundary currents, and much of the large-scale temperature structure. Part III also show that the tropical Pacific is well simulated. We are particularly pleased with the low drift found in CM2.1, where the rms temperature error is less than 1.0°C over almost half of the ocean. Such low error values are not found in CM2.0, which also has far too little ventilation in the Southern Ocean.

The differences between the two models suggest some interesting lessons about modeling the ocean circulation, some of which are explored in more detail in forthcoming papers. The strong differences in the Southern Ocean and North Pacific suggest the importance of getting the details of the wind stress field correct—thus ensuring that gyre boundaries are located in the proper locations (RGT). The sensitivity to viscosity, while relatively small, is also an interesting result since it is unclear that the large viscosities chosen for reasons

of ensuring numerical stability are physically meaningful.

The fact that the results are so sensitive to the surface wind stress reminds us that numerical improvements within the ocean alone are not sufficient to produce a more realistic climate. However, the numerical improvements made to CM2.0 do allow us to examine fields such as sea surface height and to look at the details of flow through the Arctic. The improvements in vertical resolution and advection also allow us to produce solutions where the bulk of water mass transformation occurs in the surface layers, as increasingly suggested by direct observations of turbulence and models of biogeochemistry. As can be seen in Part III, the lowering of vertical diffusion and north–south viscosity and increase in horizontal resolution in the equatorial zone allow us to produce quite realistic simulations of the Tropics. However, if the winds are in the wrong place, the hydrography will still exhibit large errors.

The similarities in errors between the two models are also interesting. The mode and intermediate waters in both hemispheres are the source of important hydrographic errors. These regions are locations that involve a balance between local cooling, eddy-driven subduction, and wind-stress-driven subduction. Additionally, both models have significant errors in hydrographic structure in both the Mediterranean Sea and northern Indian Ocean, which may be associated with the representation of dense overflows. The similarities in these errors in particular point to overflows as a key process that can be improved in future generations of the ocean model.

Acknowledgments. We thank the entire laboratory, especially our director Ants Leetmaa, for making available the support and computational resources to complete this model, and our colleagues who worked on the atmospheric and coupled model development teams. We thank Robbie Toggweiler and Sonya Legg for their reviews of this paper, and Geoff Vallis, Bob Hallberg, Alistair Adcroft, and Brian Arbic for useful discussions during the development process. The comments of two anonymous reviewers improved this manuscript. Chloroflourocarbon data were made available through the GLODAP Project.

REFERENCES

Adcroft, A., C. Hill, and J. Marshall, 1997: Representation of topography by shaved cells in a height coordinate ocean model. *Mon. Wea. Rev.,* **125,** 2293–2315.

Barry, R. G., M. C. Serreze, J. A. Maslanik, and R. H. Preller, 1993: The Arctic sea ice-climate system: Observations and modeling. *Rev. Geophys.,* **31,** 397–422.

Beckmann, A., and R. Döscher, 1997: A method for improved representation of dense water spreading over topography in geopotential-coordinate models. *J. Phys. Oceanogr.,* **27,** 581–591.

Bocaletti, G., R. Ferrari, A. Adcroft, D. Ferreira, and J. Marshall, 2005: The vertical structure of ocean heat transport. *Geophys. Res. Lett.,* **32,** L10603, doi:10.1029/2005GL022474.

Boyer, T. P., C. Stephens, J. I. Antonov, M. E. Conkright, R. A. Locarnini, T. D. O'Brien, and H. E. Garcia, 2002: *Salinity*. Vol. 2, *World Ocean Atlas 2001,* NOAA Atlas NESDIS 50, 165 pp.

Bryan, K., and L. J. Lewis, 1979: A water mass model of the world ocean. *J. Geophys. Res.,* **84,** 2503–2517.

Colony, R. L., and A. S. Thorndike, 1984: An estimate of the mean field of Arctic sea ice motion. *J. Geophys. Res.,* **89,** 623–629.

Cunningham, S. A., S. G. Alderson, B. A. King and M. A. Brandon, 2003: Transport and variability of the Antarctic Circumpolar Current in Drake Passage. *J. Geophys. Res.,* **108,** 8084, doi:10.1029/2001JC001147.

Delworth, T. L., R. J. Stouffer, K. W. Dixon, M. J. Spelman, T. R. Knutson, A. J. Broccoli, P. J. Kushner, and R. T. Wetherald, 2002: Review of simulations of climate variability and change with the GFDL R30 coupled climate model. *Climate Dyn.,* **19,** 555–574.

——, and Coauthors, 2006: GFDL's CM2 coupled climate models. Part I: Formulation and simulation characteristics. *J. Climate,* **19,** 643–674.

Doney, S. C., W. G. Large, and F. O. Bryan, 1998: Surface ocean fluxes and water-mass transformation rates in the coupled NCAR Climate System Model. *J. Climate,* **11,** 1420–1441.

——, and Coauthors, 2004: Evaluating global ocean carbon models: The importance of realistic physics. *Global Biogeochem. Cycles,* **18,** GB3017, doi:10.1029/2003GB002150.

Freeland, J., 2001: Observations of the flow of abyssal water through the Samoa Passage. *J. Phys. Oceanogr.,* **31,** 2273–2279.

Gent, P., and J. C. McWilliams, 1990: Isopycnal mixing in ocean circulation models. *J. Phys. Oceanogr.,* **20,** 150–155.

Gnanadesikan, A., 1999: A simple predictive model for the structure of the oceanic pycnocline. *Science,* **283,** 2077–2079.

——, R. D. Slater, N. Gruber, and J. L. Sarmiento, 2002: Oceanic vertical exchange and new production: A model-data comparison. *Deep-Sea Res.,* **43B,** 363–401.

——, ——, P. S. Swathi, and G. K. Vallis, 2005: The energetics of ocean heat transport. *J. Climate,* **18,** 2604–2616.

Gordon, A. L., R. D. Susanto, and K. Vranes, 2003: Cool Indonesian throughflow as a consequence of restricted surface layer flow. *Nature,* **425,** 824–828.

Griffies, S. M., 1998: The Gent–McWilliams skew flux. *J. Phys. Oceanogr.,* **28,** 831–841.

——, A. Gnanadesikan, R. C. Pacanowski, V. D. Larichev, J. K. Dukowicz, and R. D. Smith, 1998: Isopycnal mixing in a *z*-coordinate ocean model. *J. Phys. Oceanogr.,* **28,** 805–830.

——, R. C. Pacanowski, and R. W. Hallberg, 2000: Spurious diapycnal mixing associated with advection in a *z*-coordinate ocean model. *Mon. Wea. Rev.,* **128,** 538–564.

——, ——, R. M. Schmidt, and V. Balaji, 2001: Tracer conservation with an explicit free surface method for *z*-coordinate ocean models. *Mon. Wea. Rev.,* **129,** 1081–1098.

——, M. J. Harrison, R. C. Pacanowski, and A. Rosati, 2003: A technical guide to MOM 4. GFDL Ocean Group Tech. Rep.

5, NOAA/Geophysical Fluid Dynamics Laboratory, Princeton, NJ, 295 pp.

——, and Coauthors, 2005: Formulation of an ocean model for global climate simulations. *Ocean Sci.,* **1,** 45–79.

Guilyardi, E., G. Madec, and L. Terray, 2001: The role of lateral ocean physics in the upper ocean thermal balance of a coupled ocean-atmosphere GCM. *Climate Dyn.,* **17,** 589–599.

Huang, R. X., and J. Pedlosky, 2000: Climate variability induced by anomalous buoyancy forcing in a multilayer model of the ventilated thermocline. *J. Phys. Oceanogr.,* **30,** 3009–3021.

Hundsdorfer, W., and R. Trompert, 1994: Method of lines and direct discretization: A comparison for linear advection. *Appl. Numer. Math.,* **13,** 469–490.

Johns, T., and Coauthors, 2005: HadGEM1—Model description and analysis of preliminary experiments for the IPCC Fourth Assessment Report. Hadley Centre Tech. Rep. 55, Met Office, Exeter, United Kingdom, 73 pp. [Available online at http://www.metoffice.gov.uk/research/hadleycentre/pubs/HCTN/index.html.]

Johnson, G. C., D. L. Rudnick, and B. A. Taft, 1994: Bottom water variability in the Samoa Passage. *Deep-Sea Res.,* **52,** 177–196.

Large, W., J. C. McWilliams, and S. C. Doney, 1994: Oceanic vertical mixing: A review and a model with a nonlocal boundary mixing parameterization. *Rev. Geophys.,* **32,** 363–403.

——, G. Danasbogulu, J. C. McWilliams, P. R. Gent, and F. O. Bryan, 2001: Equatorial circulation of a global ocean climate model with anisotropic viscosity. *J. Phys. Oceanogr.,* **31,** 518–536.

Leaman, K. D., R. L. Molinari, and P. S. Vertes, 1987: Structure and variability of the Florida Current at 27°N: April 1982–July 1984. *J. Phys. Oceanogr.,* **17,** 565–583.

Ledwell, J. R., A. J. Watson, and C. S. Law, 1993: Evidence for slow mixing across the pycnocline from an open-ocean tracer-release experiment. *Nature,* **364,** 701–703.

——, ——, and ——, 1998: Mixing of a tracer in the pycnocline. *J. Geophys. Res.,* **103,** 21 499–21 530.

Lee, H. C., A Rosati, and M. J. Spelman, 2006: Barotropic tidal mixing effects in a coupled climate model: Oceanic conditions in the North Atlantic. *Ocean Modell.,* **11,** 464–477.

Lee, T. N., W. E. Johns, C. T. Liu, D. Zhand, R. Zantopp, and Y. Yang, 2001: Mean transport and seasonal cycle of the Kuroshio east of Taiwan with comparison to the Florida Current. *J. Geophys. Res.,* **106,** 22 143–22 158.

Levine, M. D., C. A. Paulson, and J. H. Morison, 1985: Internal waves in the Arctic Ocean: Comparison with lower-latitude observations. *J. Phys. Oceanogr.,* **15,** 800–809.

Lukas, R., and E. Firing, 1984: The geostrophic balance of the Pacific equatorial undercurrent. *Deep-Sea Res.,* **31,** 61–66.

Luyten, J. R., J. Pedlosky, and H. Stommel, 1983: The ventilated thermocline. *J. Phys. Oceanogr.,* **13,** 292–309.

Manabe, S., and K. Bryan, 1969: Climate calculations with a combined ocean-atmosphere model. *J. Atmos. Sci.,* **26,** 786–789.

——, R. Stouffer, M. Spelman, and K. Bryan, 1991: Transient responses of a coupled ocean–atmosphere model to gradual changes of atmosphere CO_2. Part I: Annual mean response. *J. Climate,* **4,** 785–818.

Marinov, I., 2004: Controls on the air-sea balance of CO_2. Ph.D. dissertation, Princeton University, 224 pp.

Matsumoto, K., and Coauthors, 2004: Evaluation of ocean carbon cycle models with data-based metrics. *Geophys. Res. Lett.,* **31,** L07303, doi:10.1029/2003GL018970.

Morel, A., and D. Antoine, 1994: Heating rate within the upper ocean in relation to its bio-optical state. *J. Phys. Oceanogr.,* **24,** 1652–1665.

Murray, R. J., 1996: Explicit generation of orthogonal grids for ocean models. *J. Comput. Phys.,* **126,** 251–273.

Orsi, A. H., T. Whitworth, and W. D. Nowlin, 1995: On the meridional extent and fronts of the Antarctic Circumpolar Current. *Deep-Sea Res.,* **42A,** 641–673.

Özgökmen, T. M., E. P. Chassignet, and C. G. H. Rooth, 2001: On the connection between the Mediterranean outflow and the Azores Current. *J. Phys. Oceanogr.,* **31,** 461–480.

Pacanowski, R. C., and A. Gnanadesikan, 1998: Transient response in a *Z*-level ocean model that resolves topography with partial cells. *Mon. Wea. Rev.,* **126,** 3248–3270.

Park, Y.-G., and K. Bryan, 2000: Comparison of thermally driven circulations from a depth-coordinate model and an isopycnal-layer model. Part I: Scaling-law sensitivity to vertical diffusivity. *J. Phys. Oceanogr.,* **30,** 590–605.

Peters, H., M. C. Gregg, and J. M. Toole, 1988: On the parameterization of equatorial turbulence. *J. Geophys. Res.,* **93** (C2), 1199–1218.

Polzin, K., 1999: A rough recipe for the energy balance of quasi-steady lee waves. *Dynamics of Internal Gravity Waves II: Proc. 'Aha Huliko'a Winter Workshop,* Honolulu, HI, University of Hawaii at Manoa, 117–128.

——, J. M. Toole, J. R. Ledwell, and R. W. Schmitt, 1997: Spatial variability of turbulent mixing in the abyssal ocean. *Science,* **276,** 93–96.

Rhein, M., L. Stramma, and U. Send, 1995: The Atlantic Deep Western Boundary Current: Water masses and transports near the equator. *J. Geophys. Res.,* **100,** 2441–2457.

Rhines, P. B., and W. R. Young, 1982: Potential vorticity homogenization in planetary gyres. *J. Fluid Mech.,* **122,** 347–367.

Ridgway, K. R., and J. R. Dunn, 2003: Mesoscale structure of the mean East Australian Current System and its relationship with topography. *Progress in Oceanography,* Vol. 56, Pergamon, 189–222.

Roach, A. T., K. Aagard, C. H. Pease, S. A. Salo, T. Weingartner, V. Pavlov, and M. Kulakov, 1995: Direct measurements of transport and water properties through Bering Strait. *J. Geophys. Res.,* **100,** 18 443–18 457.

Rothrock, D. A., J. Zhang, and Y. Yu, 2003: The arctic ice thickness anomaly of the 1990s: A consistent view from models and observations. *J. Geophys. Res.,* **108,** 3083, doi:10.1029/2001JC001208.

Rudels, B., E. P. Jones, L. G. Anderson, and G. Kattner, 1994: On the intermediate depth waters of the Arctic Ocean. *The Polar Oceans and Their Role in Shaping the Global Environment, Geophys. Monogr.,* No. 85, Amer. Geophys. Union, 33–46.

Sarmiento, J. L., T. M. C. Hughes, R. J. Stouffer, and S. Manabe, 1998: Ocean carbon cycle response to future greenhouse warming. *Nature,* **393,** 245–249.

Simmons, H. L., S. R. Jayne, L. C. St. Laurent, and A. J. Weaver, 2004: Tidally driven mixing in a numerical model of the ocean general circulation. *Ocean Modell.,* **6,** 245–263.

Sloyan, B. M., G. C. Johnson, and W. S. Kessler, 2003: The Pacific Cold Tongue: A pathway for interhemispheric exchange. *J. Phys. Oceanogr.,* **33,** 1027–1043.

Speer, K. G., S. R. Rintoul, and B. Sloyan, 2000: The diabatic Deacon cell. *J. Phys. Oceanogr.,* **30,** 3212–3222.

Stephens, C., J. I. Antonov, T. P. Boyer, M. E. Conkright, R. A. Locarnini, T. D. O'Brien, and H. E. Garcia, 2002: *Temperature*. Vol. 1, *World Ocean Atlas 2001,* NOAA Atlas NESDIS 49, 167 pp.

Stouffer, R. J., 2004: Time scales of climate response. *J. Climate,* **17,** 209–217.

——, and Coauthors, 2006: GFDL's CM2 coupled climate models. Part IV: Idealized climate response. *J. Climate,* **19,** 723–740.

Sweby, P., 1984: High-resolution schemes using flux limiters for hyperbolic conservation laws. *SIAM J. Numer. Anal.,* **21,** 995–1011.

Sweeney, C., A. Gnanadesikan, S. M. Griffies, M. Harrison, A. Rosati, and B. Samuels, 2005: Impacts of shortwave penetration depth on large-scale ocean circulation and heat transport. *J. Phys. Oceanogr.,* **35,** 1103–1119.

Talley, L. D., J. L. Reid, and P. E. Robbins, 2003: Data-based meridional overturning streamfunctions for the global ocean. *J. Climate,* **16,** 3213–3226.

Tapley, B. D., D. P. Chambers, C. K. Shum, R. J. Eanes, J. C. Ries, and R. H. Stewart, 1994: Accuracy assessment of the large-scale dynamic ocean topography from TOPEX/Poseidon altimetry. *J. Geophys. Res.,* **99** (C12), 24 605–24 617.

Tilburg, C. E., H. E. Hurlburt, J. J. O'Brien, and J. F. Shriver, 2001: The dynamics of the East Australia Current system: The Tasman Front, the East Auckland Current, and the East Cape Current. *J. Phys. Oceanogr.,* **31,** 2917–2943.

Toggweiler, J. R., and B. Samuels, 1998: On the ocean's large-scale circulation near the limit of no vertical mixing. *J. Phys. Oceanogr.,* **28,** 1832–1852.

——, R. Murnane, S. Carson, A. Gnanadesikan, and J. L. Sarmiento, 2003: Representation of the carbon cycle in box models and GCMs: 2. Organic pump. *Global Biogeochem. Cycles,* **17,** 1027, doi:10.1029/2001GB001841.

Willey, D. A., R. A. Fine, R. E. Sonnerup, J. L. Bullister, W. M. Smethie, and M. J. Warner, 2004: Global oceanic chlorofluorocarbon inventory. *Geophys. Res. Lett.,* **31,** L01303, doi:10.1029/2003GL018816.

Winton, M., 2003: On the climatic impact of ocean circulation. *J. Climate,* **16,** 2875–2889.

——, R. W. Hallberg, and A. Gnanadesikan, 1998: Simulation of density-driven frictional downslope flow in *Z*-coordinate ocean models. *J. Phys. Oceanogr.,* **28,** 2163–2174.

Wittenberg, A., and Coauthors, 2006: GFDL's CM2 global coupled climate models. Part III: Tropical Pacific climate and ENSO. *J. Climate,* **19,** 698–722.